Ultimate fate of apparent horizons during a binary black hole merger. II. The vanishing of apparent horizons

Daniel Pook-Kolb,[1,2] Ivan Booth,[3] and Robie A. Hennigar[3,4,5]

[1]*Max-Planck-Institut für Gravitationsphysik (Albert Einstein Institute), Callinstraße 38, 30167 Hannover, Germany*

[2]*Leibniz Universität Hannover, 30167 Hannover, Germany*

[3]*Department of Mathematics and Statistics, Memorial University of Newfoundland, St. John's, Newfoundland and Labrador, A1C 5S7, Canada*

[4]*Department of Physics and Astronomy, University of Waterloo, Waterloo, Ontario, Canada N2L 3G1*

[5]*Department of Physics and Computer Science, Wilfrid Laurier University, Waterloo, Ontario, Canada N2L 3C5*

(Received 30 May 2021; accepted 8 September 2021; published 25 October 2021)

In this second part of a two-part paper, we discuss numerical simulations of a head-on merger of two nonspinning black holes. We resolve the fate of the original two apparent horizons by showing that after intersecting, their world tubes "turn around" and continue backwards in time. Using the method presented in the first paper [Phys. Rev. D 084083 (2021)] to locate these surfaces, we resolve several such world tubes evolving and connecting through various bifurcations and annihilations. This also draws a consistent picture of the full merger in terms of apparent horizons, or more generally, marginally outer trapped surfaces (MOTSs). The MOTS stability operator provides a natural mechanism to identify MOTSs which should be thought of as black hole boundaries. These are the two initial ones and the final remnant. All other MOTSs lie in the interior and are neither stable nor inner trapped.

DOI: 10.1103/PhysRevD.104.084084

I. INTRODUCTION

The now numerous detections of gravitational wave events leave little doubt that black hole coalescences are a regularly occurring phenomenon in our universe [1–7]. With the help of numerical relativity simulations, the produced gravitational waves traveling to distant observers are analysed and modeled with steadily increasing efficiency and accuracy [8,9]. However, the details of the merger of the black holes themselves are less well understood. This is partly for conceptual and partly for numerical reasons.

On the conceptual side, one needs to answer the question of how to describe black holes in highly dynamical situations. When a black hole is at rest or only slightly perturbed, the event horizon is a suitable description [10]. In nonperturbative cases, however, its teleological nature makes it unsuitable for gaining an understanding of the dynamics [11–14]. A much better alternative is provided by the quasilocal horizon framework [11,15,16]. The central concept in this framework, the dynamical horizon, presents a notion of black holes that is valid and satisfies physical laws even in the highly nonlinear phases of the merger. Dynamical horizons are based on the numerically accessible marginally outer trapped surfaces (MOTSs), i.e., surfaces $\mathcal{S}$ defined as having vanishing outward expansion. Following such a MOTS through the time evolution of a spacetime generates a world tube, called a marginally outer trapped tube (MOTT). In their original definition [11,15,16], dynamical horizons are a certain subset of MOTTs. In the present work, MOTS stability [17,18] will play a central role and we shall refer to a stable MOTS as *apparent horizon*[1] (AH) and to a (section of a) MOTT foliated by apparent horizons as *dynamical apparent horizon* (DAH).

Whether we consider dynamical horizons or MOTTs in general, one seemingly basic question remained open: What happens to the horizons of two black holes when they merge? It is well known that a common apparent horizon forms around the two individual ones when they are sufficiently close to each other. This common horizon immediately splits into a stable outer and an unstable inner branch, $\mathcal{S}_{\text{outer}}$ and $\mathcal{S}_{\text{inner}}$, respectively. This fact together with the observation that MOTTs may in principle weave back and forth in time (see, e.g., [14,19]) sparked speculations that all the horizons in a binary merger might, in fact, be parts of a single world tube [20–22].

Prior to recent advances in methods for locating MOTSs numerically [23], it was not possible to further investigate these ideas. The world tubes that had to be tracked

[1]The compatibility with the traditional terminology of apparent horizons as boundaries of trapped regions will be discussed below.

developed extremely distorted shapes, which the typically used algorithms failed to resolve. The fundamental assumption often employed to simplify the numerical task is that the surface we wish to locate is star shaped, i.e., it can be represented using an angle-dependent (coordinate) distance function from some reference point. See Ref. [24] for a review.

By removing this limitation, it was shown recently in Refs. [25–28] that the individual apparent horizons $\mathcal{S}_1$ and $\mathcal{S}_2$ connect indirectly to the outer common apparent horizon $\mathcal{S}_{\text{outer}}$ in the following way. $\mathcal{S}_{1,2}$ approach each other, touch at one point at a time t_{touch} and then start to intersect. At t_{touch}, the union $\mathcal{S}_1 \cup \mathcal{S}_2$ coincides with the inner common MOTS $\mathcal{S}_{\text{inner}}$, which formed together with $\mathcal{S}_{\text{outer}}$, and which now has a cusp at the common point of $\mathcal{S}_{1,2}$. Such a non-smooth "merger" of MOTSs, or "crossing" of MOTTs, shall henceforth be referred to as *coincidence* of one MOTS with the union of two others. Immediately after the coincidence of $\mathcal{S}_{\text{inner}}$ with $\mathcal{S}_{1,2}$, $\mathcal{S}_{\text{inner}}$ develops a self-intersection. However, the later fate of the individual apparent horizons (and that of $\mathcal{S}_{\text{inner}}$) was not fully resolved in these studies. One reason for this is that in the utilized methods, one still had to anticipate the possible shapes with appropriate initial guesses. As we shall see, resolving their full fate requires even more exotic guesses, and for this a new method was needed. We have developed and presented such a method in the first paper of this two-part series, henceforth denoted as paper I [29]. As we shall see in the remainder of this second paper, having such a method is the key to resolving this question.

One might argue that in classical general relativity, whatever happens in the interior of the event horizon remains—by definition—causally disconnected from far away observers. MOTTs are always located in this interior region and, after the outer common apparent horizon has formed, the individual apparent horizons are even further away from it. Nevertheless, the question of their fate seems highly relevant if one aims at using MOTTs to understand the merger. To allow for a physically meaningful interpretation, these should be well-behaved objects in the first place. But how is this compatible with the results of paper I? There, we have shown that a two-black-hole configuration may contain a large number of MOTSs not previously known. Are these merely artifacts of an "unphysical" configuration? Since they were found in time-symmetric initial data with a common AH already present, neither the past nor the future of this configuration contains two separate black holes. In the present paper, we therefore look at the merger of initially separate black holes and aim to answer two questions: (i) Do such additional MOTSs also form dynamically in a merger of initially separate black holes? (ii) What physical significance do they have and how can we differentiate them from the intuitively more relevant apparent horizons we associate with the individual black holes ($\mathcal{S}_{1,2}$) and the final common one ($\mathcal{S}_{\text{outer}}$)?

To answer these questions, we perform numerical simulations of the head-on collision of two nonspinning black holes with no initial momentum. In particular, we show explicitly that (i) such additional MOTSs do form dynamically and (ii) the new MOTTs we track do, in fact, bifurcate and annihilate with the other MOTTs. This means that they are indeed weaving back and forth in time, but as we will see later, they do not connect to form just one single smooth surface. A remarkable result is a surprisingly clear and predictable behavior in terms of the stability of these MOTTs: Whenever a MOTT switches direction in time, it gains an additional negative eigenvalue of the stability operator, i.e., it effectively becomes "more unstable." Furthermore, only three MOTTs are stable (and hence DAHs) in the sense of [17,18] and are thus distinguished from all other MOTTs we find. These are the two DAHs traced out by $\mathcal{S}_1$ and $\mathcal{S}_2$ associated with the individual black holes and the one final common DAH traced out by $\mathcal{S}_{\text{outer}}$.

The rest of this paper is organized as follows. We start by fixing the notation and introducing the required mathematical concepts in Sec. II. Section III gives the numerical details of our setup, the simulations and the method to locate and track the marginal surfaces. The new MOTSs and the world tubes they trace out are introduced in Sec. IV. Here, we also describe a mechanism occurring multiple times along otherwise smoothly evolving MOTTs where a cusp forms followed by a new self-intersection. Additionally, we present MOTSs of toroidal topology that exist inside the individual MOTSs $\mathcal{S}_1$ and $\mathcal{S}_2$. Section V connects the various observations made in the previous sections with the MOTS stability properties. The signature and the expansion of the ingoing null rays, together important for understanding the behavior of the area, are presented in Sec. VI. Finally, Sec. VII will conclude with a discussion of the main results. This manuscript builds from the results in [29], and a summary of the main results from both papers can be found in [30].

II. BASIC NOTIONS

A. Marginal surfaces and their world tubes

We consider four-dimensional spacetime $(\mathcal{M}, g_{\alpha\beta}, \nabla_\alpha)$ with Lorentzian four-metric $g_{\alpha\beta}$ of signature $(-+++)$. For a smooth spacelike two-surface $(\mathcal{S}, q_{AB}, \mathcal{D}_A)$, let $\ell^\pm$ be two linearly independent future pointing null normals scaled such that $\ell^+ \cdot \ell^- = -1$. In the present paper we will only consider closed surfaces $\mathcal{S}$ and we assume it is possible to assign an outward direction on $\mathcal{S}$. Then, ℓ^+ is taken to be pointing outward and ℓ^- inward. The expansions $\Theta_\pm$ of a congruence of null rays traveling in the $\ell^\pm$ directions are then given by

$$\Theta_\pm = q^{\alpha\beta}\nabla_\alpha \ell^\pm_\beta, \tag{1}$$

where $q^{\alpha\beta} = e^\alpha_A e^\beta_B q^{AB}$ with e^α_A being the pull-back from $\mathcal{M}$ to $\mathcal{S}$. The expansions can be seen as the trace of the extrinsic curvatures

$$k^\pm_{AB} = \nabla_A \ell^\pm_B = e^\alpha_A e^\beta_B \nabla_\alpha \ell^\pm_\beta \tag{2}$$

of $\mathcal{S}$ associated with $\ell^\pm$. Note that since $\ell^\pm$ are orthogonal to a surface, the antisymmetric part (the twist) of $k^\pm_{AB}$ vanishes. The symmetric trace-free part of $k^\pm_{AB}$ is given by the shear

$$\sigma^\pm_{AB} = k^\pm_{AB} - \frac{1}{2}\Theta_\pm q_{AB}, \tag{3}$$

where we omitted the, in this case, unnecessary symmetrization. We will call Θ_+ the outgoing and Θ_- the ingoing expansion.

The signs of $\Theta_\pm$ allow us to classify $\mathcal{S}$. In particular, if $\Theta_\pm < 0$ then $\mathcal{S}$ is called a *trapped surface*. The existence of such a surface has been proven to imply that spacetime is causally geodesically incomplete and thus singular [31]. $\mathcal{S}$ is called a *marginally trapped surface* if $\Theta_- < 0$ and $\Theta_+ = 0$ and a *marginally outer trapped surface* (MOTS) if $\Theta_+ = 0$ with no restriction on Θ_-. We mention here that Andersson *et al.* show in [32] that existence of a strictly stable MOTS (introduced in Sec. II B) is sufficient for the singularity theorem mentioned above to hold. Note that we can still scale the null normals by arbitrary positive functions $f > 0$ via

$$\ell^+ \to f\ell^+ \quad \text{and} \quad \ell^- \to \frac{1}{f}\ell^-. \tag{4}$$

Fortunately, the signs of the expansions $\Theta_\pm$ and consequently the above characterization of $\mathcal{S}$ is invariant under these transformations.

Let the spacetime $\mathcal{M}$ be foliated by spatial slices $(\Sigma_t, h_{ij}, D_i, K_{ij})$ with Riemannian three-metric h_{ij} and extrinsic curvature K_{ij}. Following a MOTS $\mathcal{S}$ through slices of the foliation provides the notion of a MOTT. More precisely, a smooth three-manifold $\mathcal{H}$ is called a *marginally outer trapped tube* (MOTT) if it admits a foliation of MOTSs. The definition of a MOTT makes no use of the foliation of spacetime by the Σ_t. We will, however, only consider MOTTs $\mathcal{H}$ with a foliation of MOTSs contained in the slices Σ_t. For a spacelike future ($\Theta_- < 0$) MOTT $\mathcal{H}$, the foliation can be shown to be unique [33]. Note that this implies that different foliations of spacetime will in general result in finding different MOTTs. See also [15] for a discussion of this nonuniqueness.

The above objects are closely related to various terms involving the word "horizon". For instance, a spacelike future MOTT is defined as a dynamical horizon in [16,34] while in [27,28], the definition of a dynamical horizon has been generalized to refer to any MOTT. Additional qualifiers (e.g., future, spacelike) were used to then specialize where needed. One of the reasons for this generalization is that MOTSs and MOTTs were found to appear in a much wider variety than expected and the original dynamical horizon did not cover all the interesting cases. However, the examples in [27,28] were just the start and [35] showed that even in a single slice of the Schwarzschild spacetime there can be an infinite number of MOTSs. This together with the results shown in the first and this second paper clearly suggest that not all of these objects should be thought of as black hole boundaries. As mentioned in the introduction, the notion of MOTS stability turns out to reliably select those MOTSs which possess reasonable physical properties and can thus be called horizons. We will therefore introduce the MOTS stability operator in the following section.

B. MOTS stability

The concept of MOTS stability in the sense of Refs. [17,18] is helpful to get a deeper insight into the evolution properties of a MOTS. In particular, it will be useful in assessing at which time t a MOTT $\mathcal{H}$ becomes tangent to a spatial slice Σ_t and thus generically "turns around" in time. These instances correspond to a MOTT appearing and bifurcating into two branches, as well as when two MOTTs merge and annihilate. Furthermore, we expect the physically relevant horizons to be boundaries for trapped and untrapped surfaces, at least in a neighborhood. This property also turns out to be closely related to the notion of MOTS stability.

Before delving into the fully generic case, it will be helpful to first consider a very simple situation in which the stability operator appears almost naturally. Spherically symmetric spacetimes provide such an example and so here we restrict our attention to spherically symmetric MOTSs.

1. MOTTs in spherical symmetry

We will start by establishing some basic properties of MOTTs in spherical symmetry. In this setting, each point in the two-dimensional (t, r) space represents a sphere and we can calculate its expansion Θ_+. A point (t, r) can then be labeled as outer trapped, outer untrapped or marginally outer trapped as shown in Fig. 1. A MOTT $\mathcal{H}$ traces a curve through the (t, r) space and it can weave its way back and forth through the foliation of spacetime.

Tangents to this curve can be written in the form

$$\mathcal{V}^\alpha = \mathcal{N}(u^\alpha + w n^\alpha), \tag{5}$$

where u^α and n^α are respectively the unit vectors in the t and r directions. $\mathcal{N}$ can be any function of (t, r), though a convenient choice is the lapse. w is the speed of $\mathcal{H}$ relative to the foliation. $\mathcal{H}$ is spacelike if $|w| > 1$, timelike if $|w| < 1$ and null if $|w| = 1$. If $\mathcal{H}$ becomes tangent to the foliation (as at B or C) then at that point $|w| \to \infty$.

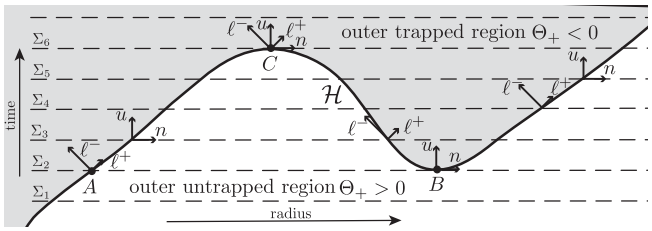

FIG. 1. Spherically symmetric evolution of a MOTT $\mathcal{H}$ (thin solid line). It is perfectly possible for $\mathcal{H}$ to weave back and forth through the time foliation. See, for example, [19,20] for exact solutions exhibiting this behavior.

The speed w may also be calculated from the fact that $\Theta_+ = 0$ on $\mathcal{H}$. Then writing the derivative in the $\mathcal{V}$ direction as $\delta_\mathcal{V}$ (the notation is chosen to be compatible with the next section), $\delta_\mathcal{V}\Theta_+ = 0$. It follows that

$$w = -\frac{\delta_u\Theta_+}{\delta_n\Theta_+} = 1 - 2\frac{\delta_{\ell^+}\Theta_+}{\delta_n\Theta_+}, \tag{6}$$

where we made a particular choice for the null vectors[2] relative to u and n:

$$\ell^+ = \frac{1}{2}(u+n) \quad \text{and} \quad \ell^- = u - n. \tag{7}$$

Then we can again see that if $\delta_n\Theta_+ \to 0$, $|w| \to \infty$ (as long as $\delta_{\ell^+}\Theta_+ \neq 0$).

Next, applying the spherically symmetric null Raychaudhuri equation we find

$$w = 1 + 2\frac{G_{++}}{\delta_n\Theta_+}. \tag{8}$$

By the null energy condition, $G_{++} = G_{\alpha\beta}\ell^\alpha_+\ell^\beta_+ \geq 0$. If it vanishes, then $w = 1$ and so $\mathcal{H}$ is outward null and isolated at that point. If matter falls through $\mathcal{H}$ ($G_{\alpha\beta}\ell^\alpha_+\ell^\beta_+ > 0$) and the region outside of $\mathcal{H}$ is outer untrapped (from A to C and then B onwards in Fig. 1) then $\delta_n\Theta_+ > 0 \Rightarrow w > 1$ and $\mathcal{H}$ is spacelike outward at that point. However if the region outside of $\mathcal{H}$ is outer trapped (from C to B) then $\delta_n\Theta_+ < 0$ and so $\mathcal{H}$ could be either spacelike, timelike or (inward) null. At C it transitions from $w = \infty$ to $-\infty$ and at B from $-\infty$ to ∞.

These quantities also determine the behavior of the area of $\mathcal{H}$. From (5) and (8)

$$\Theta_\mathcal{V} = \mathcal{N}(\Theta_u + w\Theta_n) = -\left(\frac{G_{++}}{\delta_n\Theta_+}\right)\Theta_-, \tag{9}$$

where $\Theta_\mathcal{V} = q^{\alpha\beta}\nabla_\alpha\mathcal{V}_\beta$ and Θ_u, Θ_n analogously. Thus if $G_{++} = 0$, then $\Theta_\mathcal{V} = 0$ and $\mathcal{H}$ does not change in area. However if $G_{++} \neq 0$ and $\Theta_- < 0$ (that is, the (t, r) spheres get smaller moving inward from the MOTT), then the area of $\mathcal{H}$ is increasing if the region just outside is outer untrapped (from A to C and then B onwards) and decreasing if the region outside of $\mathcal{H}$ is outer trapped (from C to B). Together these results mean that if we consider $\mathcal{H}$ as a continuous curve running in the direction A to B then it is always increasing in area as one would expect for a black hole horizon.

Note that the exact location of the transition points is at least partly a function of the foliation. For example, if we chose a foliation rotated relative to our original Σ_t in Fig. 1, then the points of tangency between $\mathcal{H}$ and the foliation would be different. Their number could even increase. However the possible timelike signature of $\mathcal{H}$ means that this wending through time cannot (always) be understood as simply a by-product of the choice of spacetime foliation. Timelike sections necessarily intersect with many slices of any foliation.

Finally note that a simulation that only tracked outermost MOTSs would see an apparent horizon jump from A to B at Σ_2. However a more careful tracker would identify B as a MOTS pair creation event with one surface subsequently moving inwards while the other travels outwards. Ultimately that inward moving MOTS would annihilate with the original apparent horizon at C. Both pair creation and annihilation events happen at points where $\delta_n\Theta_+ \to 0$.

2. The MOTS stability operator

Away from spherical symmetry everything is more complicated, though many of the themes (and conclusions) that we have just examined remain. In particular $\delta_n\Theta_+$ continues to play a key role though it is now generalized to become the MOTS stability operator [17,18].

Leaving rigid spherical symmetry behind, there is no longer just one way to deform a surface outwards (or inwards). Since deformations tangent to a MOTS $\mathcal{S}$ leave Θ_+ invariant, we will only consider deformations along some direction V^α normal to $\mathcal{S}$. In principle, this normal need not be limited to a particular slice Σ_t containing $\mathcal{S}$ and hence V^α may have a component pointing away from Σ_t. We will later restrict V^α to be proportional to the normal n^α of $\mathcal{S}$ within the slice Σ_t. Now, for a deformation of $\mathcal{S}$ along V^α, consider a family $\mathcal{S}_v$ of similar surfaces such that $\mathcal{S}_0 = \mathcal{S}$. Points $p \in \mathcal{S}$ then trace out curves $\gamma_p(v)$ and we take the family $\mathcal{S}_v$ such that the tangents $\frac{\partial}{\partial v}$ to these curves satisfy

$$\frac{\partial}{\partial v} = \Psi V \tag{10}$$

for a function Ψ. Note that for a fixed normal V^α the local deformation of $\mathcal{S}$ is fully determined by Ψ as a function on

[2]A specialization to these same normals is made in Eq. (5) of paper I [29] and overbars are included to indicate that a specific scaling has been chosen. However in this paper we work only with this specific choice and so for notational simplicity we omit the overbars on $\ell^\pm$ and dependent quantities.

just $\mathcal{S}$. For the spherical deformations of the last section, Ψ would be a constant and V^α would be the normal n^i in a $t = \text{const}$ slice.

Next, to each of the $\mathcal{S}_v$ we can construct a (nonunique) pair of null normals $\ell_v^\pm$ and calculate the expansions $\Theta_\pm^v$. They are chosen so that $\ell_0^\pm = \ell^\pm$ (the original null normals on $\mathcal{S}$). The MOTS stability operator L_V with respect to the normal V^α, scaled[3] such that $V^\alpha \ell_\alpha^+ = 1$, is then defined as the derivative of Θ_+^v with respect to v:

$$L_V \Psi \coloneqq \delta_{\Psi V} \Theta_+ \coloneqq \left.\frac{\partial}{\partial v}\right|_{v=0} \Theta_+^v. \tag{11}$$

It is shown in [18] that L_V does not depend on the choice of $\ell_v^\pm$ away from $\mathcal{S}$. On the other hand, the definition of L_V is not invariant under the rescalings (4) of the null normals $\ell^\pm$. However, since we will be interested only in its eigenvalues, we can use the fact that L_V is isospectral under (4) as shown in [36] and we shall work with the particular choice (7).

Just as in the spherical case of the previous section, we will discuss the evolution properties of a MOTT $\mathcal{H}$ in the context of some fixed foliation Σ_t and use this foliation to talk about *bifurcations* and *annihilations*. We will then need to choose the vector V^α as the normal of $\mathcal{S}$ which lies in Σ_t, i.e., we choose[4] $V^\alpha = 2n^\alpha$. The stability operator with respect to the slice Σ_t is then defined as $L_\Sigma \Psi \coloneqq L_{2n^\alpha} \Psi$ and it takes the form (e.g., [17,18,37]):

$$L_\Sigma \Psi = -\triangle \Psi + \left(\frac{1}{2}\mathcal{R} - 2|\sigma_+|^2 - 2G_{++} - G_{+-}\right)\Psi, \tag{12}$$

where factors of 2 differing from [17,18] result from our different cross normalization $\ell^+ \cdot \ell^- = -1$ and where

$$\triangle \Psi = (\mathcal{D}_A - \omega_A)(\mathcal{D}^A - \omega^A)\Psi \tag{13}$$

with $\omega_A = -e_A^\alpha \ell_\beta^- \nabla_\alpha \ell_+^\beta$ the connection on the normal bundle of $\mathcal{S}$, $\mathcal{R}$ its Ricci scalar, $G_{+-} = G_{\alpha\beta}\ell_+^\alpha \ell_-^\beta$, $G_{++} = G_{\alpha\beta}\ell_+^\alpha \ell_+^\beta$ and $|\sigma_+|^2 = \sigma_{AB}^+ \sigma_+^{AB}$. This is a second order, linear, elliptic operator with discrete spectrum and for a nonvanishing connection ω_A it is not self-adjoint. However, its principal eigenvalue λ_0, i.e., the eigenvalue with the smallest real part, is always real. A MOTS $\mathcal{S}$ with $\lambda_0 \geq 0$, $\lambda_0 > 0$, $\lambda_0 < 0$ is called *stable*, *strictly stable*, or *unstable*, respectively. The meaning of this terminology will soon become clear.

[3]In particular, V cannot be parallel to ℓ^+.

[4]The factor 2 results from our different convention (7) for the scaling of ℓ^+ as compared to [17]. However, this does not change the spectrum of L_V.

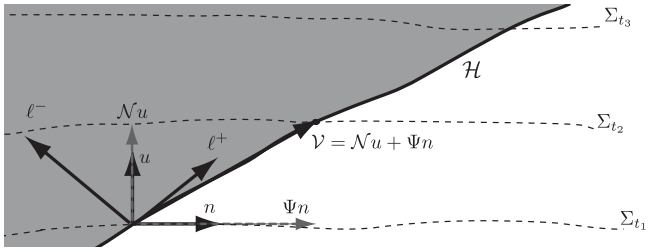

FIG. 2. Definition of the evolution vector $\mathcal{V}$ along a MOTT $\mathcal{H}$. $\mathcal{V}$ can be split into a component Ψn orthogonal to $\mathcal{S} = \mathcal{H} \cap \Sigma_{t_1}$ within Σ_{t_1} and one orthogonal to Σ_{t_1}, i.e., $\mathcal{N}u$, which is also orthogonal to $\mathcal{S}$.

Note that for the spherical cases that we considered in the last section, $\omega_A = 0$ and $\sigma_{AB}^+ = 0$ and we were only considering constant Ψ. With those restrictions

$$L_\Sigma \Psi = 2\delta_{\Psi n}\Theta_+ = \left(\frac{1}{R^2} - 2G_{++} - G_{+-}\right)\Psi, \tag{14}$$

where R is the areal radius of the MOTS. Then the term in parentheses is the principal[5] eigenvalue of L_Σ. Hence in spherical symmetry we can only have an "ingoing" $\mathcal{H}$ when the sum of the matter terms is comparable in size to $1/R^2$. If it is not then, as we saw earlier, $\mathcal{H}$ is necessarily spacelike and (if $\Theta_- < 0$) growing in area. However if it is equal so that $\delta_{\Psi n}\Theta_+ = 0$, then we can have horizon pair formation (annihilation) as at B (C) in Fig. 1. Physically this can be thought of as a case where the matter outside is dense enough to cause the formation of a new horizon outside the old one [20].

Returning to the general stability operator (12), Andersson *et al.* proved in [17,18] that $\lambda_0 > 0$ implies existence of a smooth MOTT $\mathcal{H}$ containing $\mathcal{S}$. That is, $\mathcal{S}$ evolves smoothly to the future and to the past for at least a short time interval. This can be understood intuitively in the following way. Consider a three-dimensional MOTT $\mathcal{H}$ in spacetime, illustrated in Fig. 2. Again, let $\mathcal{V}^\alpha$ be the tangent to $\mathcal{H}$ orthogonal to the MOTSs $\mathcal{S}$ and scaled such that $\mathcal{L}_\mathcal{V} t = 1$, where $\mathcal{L}_\mathcal{V}$ is the Lie-derivative along $\mathcal{V}^\alpha$. For a fixed foliation Σ_t, we can split $\mathcal{V}^\alpha$ into the components orthogonal and tangent to Σ_t,

$$\mathcal{V}^\alpha = \mathcal{N}u^\alpha + \Psi n^\alpha, \tag{15}$$

where the foliation fully determines the lapse $\mathcal{N}$ and so $\mathcal{N}u^\alpha$ is fixed. Clearly, the variation of the expansion along the MOTT $\mathcal{H}$ vanishes,

[5]Allowing nonconstant Ψ would add a term $-\Delta_\mathcal{S}\Psi$, where $\Delta_\mathcal{S}$ is the Laplacian on $\mathcal{S}$. The spectrum would then be that of the Laplacian on a round sphere (with lowest eigenvalue being zero) shifted by the constant term in parenthesis in Eq. (14).

$$\delta_{\mathcal{V}}\Theta_+ = 0, \tag{16}$$

which means that finding the tangent vector $\mathcal{V}^\alpha$ amounts to solving the inhomogeneous partial differential equation

$$L_\Sigma \Psi = -2\delta_{\mathcal{N}u}\Theta_+ \tag{17}$$

for Ψ. The inhomogeneity on the right-hand side of this is fixed by the foliation.

Note that if L_Σ is invertible, then there exists a solution for (17) for *any* lapse $\mathcal{N}$. This is guaranteed if, e.g., $\lambda_0 > 0$. However, if $\lambda_0 \leq 0$, then invertibility can fail, as eigenvalues may vanish. Equivalently, in that case there are homogeneous solutions to the evolution equation (17): that is we can choose a $\mathcal{V}^\alpha$ that is tangent to Σ_t and still satisfies (16). The pair creation event B in Fig. 1 is such an event. This association of vanishing eigenvalues with pair creation/annihilation has also been observed away from spherical symmetry [23]. In the present paper, we shall see multiple instances of MOTTs appearing and vanishing precisely as one of the eigenvalues—not necessarily λ_0—becomes zero. If it is λ_0 that vanishes, then Proposition 5.1 of [32] shows that generically $\mathcal{H}$ is tangent to Σ_t and, for fixed slicing, unique at least in a neighborhood.

Note too that $\lambda_0 > 0$ implies that $\delta_{\Psi n}\Theta_+ > 0$ and again, just as we saw in the spherically symmetric case, this is sufficient to imply that the evolving $\mathcal{H}$ is spacelike at that point [17,18] and so, if $\Theta_- < 0$, increasing in area (see also [34,38]). This area increase theorem has been generalized to include timelike "backwards in time" segments [39]. However this is not the end of the story: certain assumptions made in that generalized proof have now been shown to not always hold during black hole mergers [27,28]. We will see further examples of this in Sec. VI.

Stability is not only useful for understanding the evolution of $\mathcal{H}$, it also tells us something about local properties of $\mathcal{S}$ *within* the slice Σ_t. In paper I, it is shown that the stability operator for MOTSs can be understood as the analogue of the Jacobi operator for geodesics [29]. Thus if one considers an axisymmetric MOTS to be one of a congruence of marginally outer trapped (possibly open) surfaces, then the number of negative eigenvalues of the stability operator corresponds to the number of intersections with other nearby members of the congruence. Hence a stable MOTS with $\lambda_0 > 0$ does not intersect its neighbors while an unstable one certainly does have such intersections.

More generally, it is shown in [17,18] that a strictly stable MOTS $\mathcal{S}$ ($\lambda_0 > 0$) has the *barrier property*. In essence, this means that given a close-by surface $\mathcal{S}'$ then if $\mathcal{S}'$ has expansion $\Theta'_+ \leq 0$, it cannot extend into the exterior of $\mathcal{S}$. Similarly if $\Theta'_+ \geq 0$, it cannot enter the interior. On the other hand if $\mathcal{S}$ has the barrier property, it is at least stable.

Following from these results, we adopt the following convention in the present work. A stable MOTS $\mathcal{S}$ shall be called an *apparent horizon* (AH). Note that an apparent horizon is usually defined as the outer boundary of the trapped region in a given slice Σ_t. Due to Theorem 2.1 in [32], this boundary is a stable MOTS, so our definition includes the previous one and extends it to include surfaces that can still reasonably be associated with black hole boundaries. Examples are the previously outermost MOTSs $\mathcal{S}_1$ and $\mathcal{S}_2$, as we shall see below.

Similarly, a section of a MOTT $\mathcal{H}$ will be called a *dynamical apparent horizon* (DAH) if it allows a foliation by apparent horizons. As we saw in the preceding discussion, it is common for MOTTs identified during evolutions to include both stable (DAH) and unstable regions.

3. Simplification for vacuum, axial symmetry, and no spin

As shown in the first paper, for nonspinning axisymmetric MOTSs $\mathcal{S}$ in vacuum, we can simplify L_Σ to

$$L_\Sigma \Psi = -\Delta_{\mathcal{S}}\Psi + \left(\frac{1}{2}\mathcal{R} - 2|\sigma_+|^2\right)\Psi, \tag{18}$$

where $\Delta_{\mathcal{S}} = \mathcal{D}_A\mathcal{D}^A$ is the Laplacian on $\mathcal{S}$. In this case L_Σ is self-adjoint with purely real spectrum. Another simplification can be made if we introduce coordinates (θ, ϕ) on $\mathcal{S}$. Let ϕ be the coordinate along orbits of the axial Killing field φ^A preserving the two-metric q_{AB} and vanishing at exactly two points, the poles of $\mathcal{S}$. We take ϕ to be in the range $[0, 2\pi)$. Let further θ be any coordinate orthogonal to ϕ, e.g., $\cos\theta = \zeta$, with ζ constructed as in Ref. [40]. Then we can write any eigenfunction Ψ of L_Σ as

$$\Psi(\theta, \phi) = \sum_{m=-\infty}^{\infty} \Psi_m(\theta) e^{im\phi}. \tag{19}$$

For each $m \in \mathbb{Z}$, the eigenvalue problem $L_\Sigma\Psi = \lambda\Psi$ then reduces to a one-dimensional problem

$$L_\Sigma^m \Psi_m \coloneqq (L_\Sigma + m^2 q^{\phi\phi})\Psi_m = \lambda\Psi_m. \tag{20}$$

The eigenvalues of Eq. (20) are labeled as $\lambda_{l,m}$, where l is chosen to run from $l = |m|$ over the eigenvalues in ascending order. This guarantees that for a round sphere, for which the spectrum reduces to that of the Laplacian on a sphere of radius R_0 and shifted by $\frac{1}{2}\mathcal{R} = 1/R_0^2$, the eigenvalues are labeled in the conventional way as $\lambda_{l,m} = (1 + l(l+1))/R_0^2$. For brevity, we will sometimes write $\lambda_l \coloneqq \lambda_{l,0}$.

III. NUMERICAL SETUP AND MOTS FINDING

We use Brill-Lindquist initial data [41] for our simulations. These describe a Cauchy slice Σ which is time symmetric, i.e., with vanishing extrinsic curvature.

The topology of Σ is $\mathbb{R}^3\backslash\{x_1, x_2\}$, where $x_{1,2}$ are the coordinates of two punctures. The Riemannian three-metric is conformally flat, $h_{ij} = \psi^4\delta_{ij}$, where δ_{ij} is the flat metric. The conformal factor is given by

$$\psi = 1 + \frac{m_1}{2r_1} + \frac{m_2}{2r_2}, \tag{21}$$

where $m_{1,2}$ are the bare masses of the black holes and $r_{1,2}$ are the (coordinate) distances to the respective puncture. We shall here focus primarily on one particular configuration with total ADM mass $M = m_1 + m_2 = 1$ and a mass ratio of $q = m_2/m_1 = 2$ (i.e., $m_1 = 1/3$, $m_2 = 2/3$). We choose a distance parameter of $d \coloneqq ||x_2 - x_1||_2 = 0.9$ resulting in two black holes which are initially separate with no common apparent horizon present.

We track the various MOTSs in the simulations using the method described in [23,26] and available from [42], which in turn uses software libraries described in [43–50]. The first step in tracking a MOTS with this method is to provide an initial guess surface in order to find the MOTS in one time slice. From that point, the MOTS can be tracked backwards and forwards through the foliation. Of course, the initial guess surface can itself be a MOTS, and we use two approaches to locate the new MOTSs for this purpose. One is the shooting method described in paper I [29], which can, in principle, locate all axisymmetric MOTSs of spherical topology by choosing suitable starting points on the z-axis. This method has been implemented in [42] and can be applied to both analytically known initial data as well as to slices obtained, e.g., from numerical simulations. The other method is motivated by the assumption that MOTSs may vanish and appear only in pairs of two. Based on this idea, we try to track each MOTS to the future and to the past. Whenever a MOTS cannot be tracked further in either direction, we look for a "close by" one with which it might merge. Such a merger will be an annihilation if it happens to the future and a bifurcation if it happens in the past direction. Appendix A details the method we use to locate such a corresponding MOTT using families of surfaces of constant expansion Θ_+.

The simulations themselves are carried out using the Einstein Toolkit [51,52]. The Brill-Lindquist initial data are generated by TwoPunctures [53], while we use an axisymmetric version of McLachlan [54] for evolving these data in the BSSN formulation of the Einstein equations. This uses Kranc [55,56] to generate efficient C++ code. We always work with the $1 + \log$ slicing and a Γ-driver shift condition [57,58]. An important feature of these gauge conditions is that they are "singularity avoiding," which results in simulation time effectively slowing down close to the punctures. It was seen in [59] that the individual MOTTs $\mathcal{S}_{1,2}$ essentially stop evolving due to this effect, with the precise behavior being highly dependent on the choice of initial data: A smaller initial distance allows the $\mathcal{S}_{1,2}$ to evolve further during the simulation. We repeat our simulations at different resolutions to ensure convergence of our results. Most of these results are obtained using a spatial grid resolution of $1/\Delta x = 720$, with additional simulations carried out with $1/\Delta x = 240$, 360, and 480. Shorter simulations to verify certain features were performed at $1/\Delta x = 960$ and 1920. We do not use mesh refinement and choose our domain large enough to ensure that any boundary effects do not reach the MOTSs for as long as we track them. Additional details and convergence properties of our simulations are described in Ref. [26].

IV. OVERVIEW OF THE VARIOUS MOTTS

The general picture one expects to find in head-on mergers of two black holes has previously been analyzed in great detail [25–28,60–62]: Initially, only two individual apparent horizons are present, $\mathcal{S}_1$ and $\mathcal{S}_2$, belonging to the two separate black holes. At a time $t^{\text{outer}}_{\text{bifurcate}}$, common MOTSs $\mathcal{S}_{\text{outer}}$ and $\mathcal{S}_{\text{inner}}$ form as one surface and bifurcate into two branches. While $\mathcal{S}_{\text{outer}}$ settles to the final Schwarzschild horizon, $\mathcal{S}_{\text{inner}}$ travels inwards and becomes increasingly distorted. At the precise time when $\mathcal{S}_{1,2}$ touch, denoted as t_{touch}, $\mathcal{S}_{\text{inner}}$ forms a cusp and coincides with $\mathcal{S}_1 \cup \mathcal{S}_2$. Immediately afterwards, $\mathcal{S}_{1,2}$ intersect each other while $\mathcal{S}_{\text{inner}}$ forms self-intersections. However, the final fate of $\mathcal{S}_1$, $\mathcal{S}_2$ and $\mathcal{S}_{\text{inner}}$ had not been resolved in those studies. We shall attempt to resolve that fate here.

In the following, we will encounter several new MOTSs $\mathcal{S}$ and we will, as before, differentiate between them using different sub- and superscripts. It is understood that replacing "$\mathcal{S}$" with "$\mathcal{H}$" indicates that we refer to the MOTT traced out by $\mathcal{S}$.

A. Area evolution

The main results are most easily visualized in terms of the area of the various MOTSs. Figure 3 shows that we indeed find multiple new MOTSs previously not known, each forming in a bifurcation as a pair with an *outer* and an *inner* branch. Furthermore, we find MOTSs which merge and annihilate in pairs of two. Each bifurcation and annihilation connects two MOTTs in a locally smooth world tube. Upon formation, the area of the outer branch increases while it decreases for the inner branch. However, with the exception of $\mathcal{S}_{\text{outer}}$, even the areas of the outer branches soon start to decrease. This nonmonotonic behavior of the area along a smooth portion of a MOTT has been previously discussed for $\mathcal{S}_{\text{inner}}$ in [25,27] and has been attributed to properties of the expansion Θ_- of the ingoing null rays ℓ^- and to the signature of the world tube. We shall here extend the discussion of these properties to the new world tubes in Sec. VI. One characteristic that all MOTSs $\mathcal{S}$ along such a MOTT have in common is which punctures

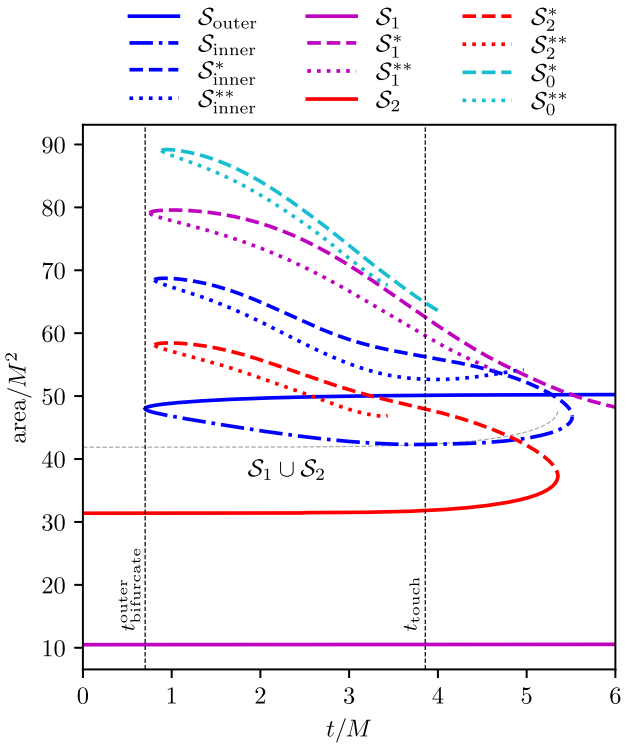

FIG. 3. Evolution of the area of the various MOTSs. Lines of the same color and different line styles smoothly connect and correspond to a single world tube continuing back and forth in time (except for the pair $(\mathcal{S}_1, \mathcal{S}^{*}_1)$, which is discussed in Sec. IV B 3). The sum of the areas of $\mathcal{S}_{1,2}$ is shown as the thin dashed line. This agrees with the area of $\mathcal{S}_{\rm inner}$ at $t_{\rm touch}$ marking the coincidence of $\mathcal{S}_{\rm inner}$ with $\mathcal{S}_1 \cup \mathcal{S}_2$. Note that despite some MOTSs having larger area than $\mathcal{S}_{\rm outer}$, they are, in fact, all contained within $\mathcal{S}_{\rm outer}$ for $t \geq t^{\rm outer}_{\rm bifurcate}$. For all curves that end without smoothly connecting to another curve, we lost track of the corresponding MOTS for numerical reasons (see the end of Sec. IV A for details).

they enclose, i.e., no MOTS crosses a puncture in its evolution. Further, all additional bifurcations happen *after* (with respect to simulation time) the formation of the outermost common MOTS $\mathcal{S}_{\rm outer}$ at $t^{\rm outer}_{\rm bifurcate}$ and the new MOTSs are solely contained within $\mathcal{S}_{\rm outer}$.

We note here that we lose track of some of the MOTSs, such as $\mathcal{S}^{**}_2$, during the simulation without having an indication of an annihilation. The reason we cannot track these MOTSs further is a purely numerical one. The shapes move very close to one of the punctures in our numerical coordinates (the proper distance to the puncture is, of course, always infinite). This close proximity results in loss of numerical accuracy since a large spatial region is covered by a decreasing number of numerical grid points as the puncture is approached, i.e., this region is numerically underresolved. Fortunately, the analysis of the MOTS stability spectrum enables us to clearly differentiate between a MOTS vanishing due to annihilation and one vanishing due to loss of accuracy.

B. The world tubes

In this subsection, we will give an overall description of the individual connected world tubes.

1. The world tube of $\mathcal{S}_{\rm outer}$

The most complicated of the four world tubes is the one that asymptotes to the final Schwarzschild horizon. Starting with $\mathcal{S}_{\rm outer}$, this MOTT is composed of the sequence $\mathcal{S}_{\rm outer} \to \mathcal{S}_{\rm inner} \to \mathcal{S}^{*}_{\rm inner} \to \mathcal{S}^{**}_{\rm inner}$. All MOTSs along this MOTT enclose both punctures. Figure 4 shows several examples of these MOTSs as we follow this world tube, starting with $\mathcal{S}_{\rm outer}$ (top left panel) and moving backwards. We find the well-known bifurcation of $(\mathcal{S}_{\rm outer}, \mathcal{S}_{\rm inner})$ at $t^{\rm outer}_{\rm bifurcate} \approx 0.702M$ (top center panel). Going now forward in time along the inner common MOTT $\mathcal{H}_{\rm inner}$, we find that $\mathcal{S}_{\rm inner}$ coincides momentarily with $\mathcal{S}_1 \cup \mathcal{S}_2$ at $t_{\rm touch} \approx 3.86M$ (middle left panel) and afterwards develops self-intersections. It merges and annihilates smoothly with $\mathcal{S}^{*}_{\rm inner}$, which retains the self-intersection, and travels from the annihilation backwards in time until shortly after $t^{\rm outer}_{\rm bifurcate}$ (bottom left panel). At this point, it smoothly connects to $\mathcal{S}^{**}_{\rm inner}$ in a bifurcation. $\mathcal{S}^{**}_{\rm inner}$, initially fully outside and enclosing $\mathcal{S}_2$, subsequently becomes increasingly distorted. Just like $\mathcal{S}_{\rm inner}$, it forms a cusp at the time $t^{\rm inner^{**}}_{\rm cusp}$ when the lower part of it passes from the outside to the inside of $\mathcal{S}_2$, after which it has a second self-intersection (bottom right panel of Fig. 4, see also Fig. 10).

The two instances where a cusp is formed along this MOTT are very similar in nature. An important ingredient for understanding these is the maximum principle for MOTSs (c.f. Sec. 3.2 in [21]). This implies that two smooth MOTSs $\mathcal{S}$ and $\mathcal{S}'$, one enclosing the other, must be identical if they have a common point with normals pointing in the same direction. This is precisely the situation of $\mathcal{S}_{\rm inner}$ as it approaches $t_{\rm touch}$ and that of $\mathcal{S}^{**}_{\rm inner}$ as $t \to t^{\rm inner^{**}}_{\rm cusp}$. As the common MOTS ($\mathcal{S}_{\rm inner}$ or $\mathcal{S}^{**}_{\rm inner}$, respectively) passes from the outside to the inside of one of the enclosed MOTSs, there is inevitably a coincidence of points, e.g., on the z-axis with normals pointing in the same direction. Then by the maximum principle the common MOTS must agree with the enclosed one.

To now understand the cusp formation, consider first the case of $\mathcal{S}_{\rm inner}$ passing through $\mathcal{S}_1$. The common MOTS $\mathcal{S}_{\rm inner}$ encloses both $\mathcal{S}_1$ and $\mathcal{S}_2$. Since $\mathcal{S}_1$ and $\mathcal{S}_2$ are not contained within *each other*, $\mathcal{S}_{\rm inner}$ cannot coincide with just $\mathcal{S}_1$ if it has a continuous evolution. For if that were the case, it would have to first pass through (and hence coincide with) $\mathcal{S}_2$ in order to be close to $\mathcal{S}_1$ everywhere. What happens instead is that $\mathcal{S}_{\rm inner}$ momentarily becomes nonsmooth and coincides with $\mathcal{S}_1 \cup \mathcal{S}_2$ at the precise time when they touch and have one common point. This allows for a continuous evolution of $\mathcal{S}_{\rm inner}$. The numerical evidence for this scenario has been presented previously in Refs. [25,26].

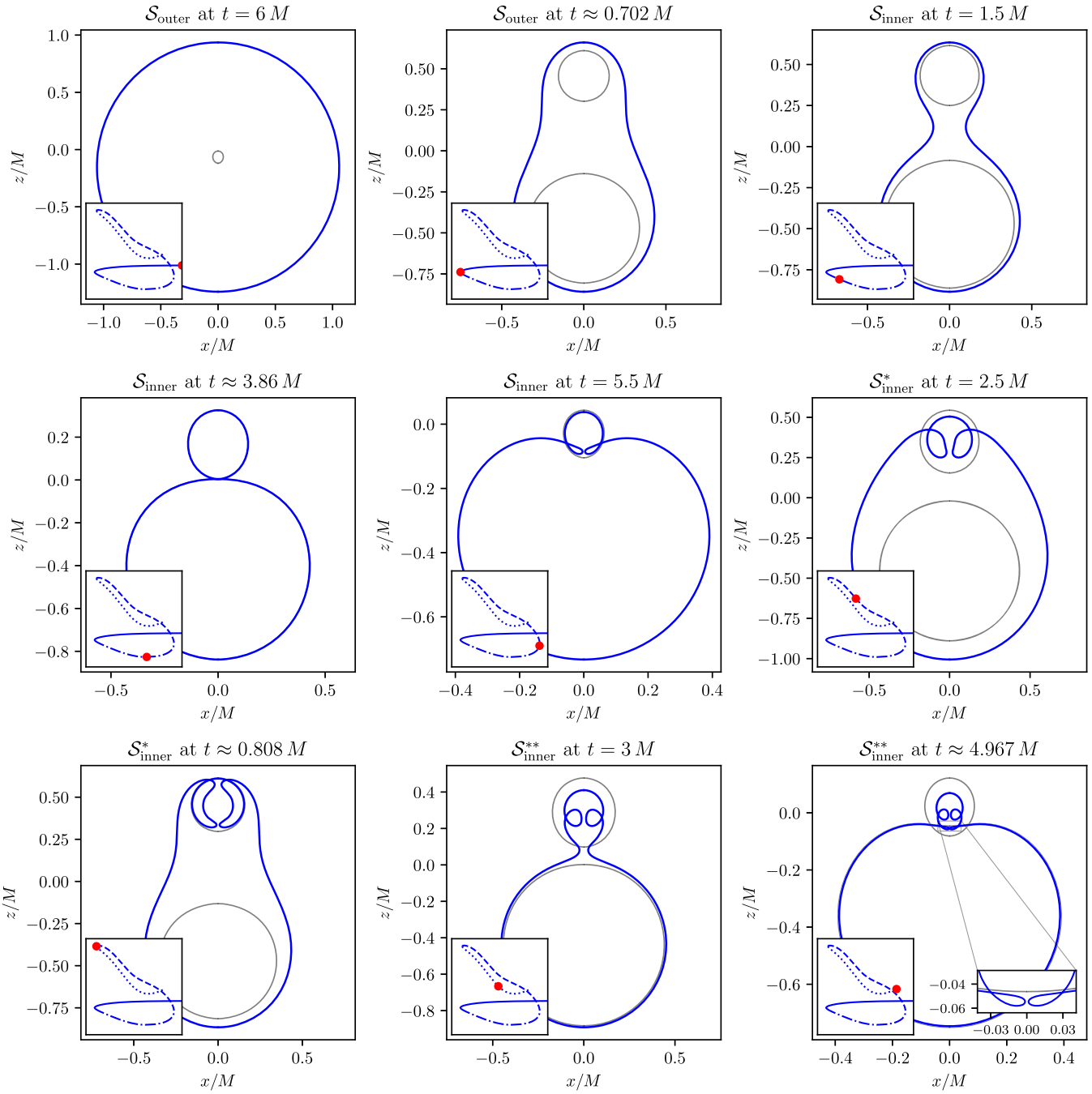

FIG. 4. Several shapes of the MOTSs along the connected MOTT following the sequence $\mathcal{S}_{\text{outer}} \to \mathcal{S}_{\text{inner}} \to \mathcal{S}^{*}_{\text{inner}} \to \mathcal{S}^{**}_{\text{inner}}$. The panels are to be read row by row from left to right. The respective inset in the bottom-left indicates the location of the shown MOTS on the connected area curve with a red dot (see Fig. 3 for the precise axes and labels). For reference, the shapes of $\mathcal{S}_1$ and $\mathcal{S}_2$ are drawn as light gray solid lines (except for the top-left and the center panel, where $\mathcal{S}_2$ does not exist). We start in the top-left panel with $\mathcal{S}_{\text{outer}}$ at $t = 6M$ and then repeatedly go backwards and forwards, following the MOTT until we reach $\mathcal{S}^{**}_{\text{inner}}$ at the final time $t \approx 4.967M$ at which it could be located (bottom-right panel). The inset in the bottom-right of this last panel shows the newly formed second self-intersection of $\mathcal{S}^{**}_{\text{inner}}$.

Similarly, $\mathcal{S}^{**}_{\text{inner}}$ momentarily coincides with $\mathcal{S}_2$ and at that moment has a cusp. The other MOTS it coincides with is $\mathcal{S}_{1c}$, which is discussed in Sec. IV C. Below, we will see further examples of such coincidences of one MOTS with the union of two others.

2. The world tube of $\mathcal{S}_2$

This MOTT consists of the sequence $\mathcal{S}_2 \to \mathcal{S}^{*}_2 \to \mathcal{S}^{**}_2$, with MOTSs shown in Fig. 5. Starting with $\mathcal{S}_2$ at $t = 0$ (top left panel), we find the annihilation of $\mathcal{S}_2$ with $\mathcal{S}^{*}_2$ at $t \approx 5.352M$ (top center panel). $\mathcal{S}^{*}_2$ is then followed

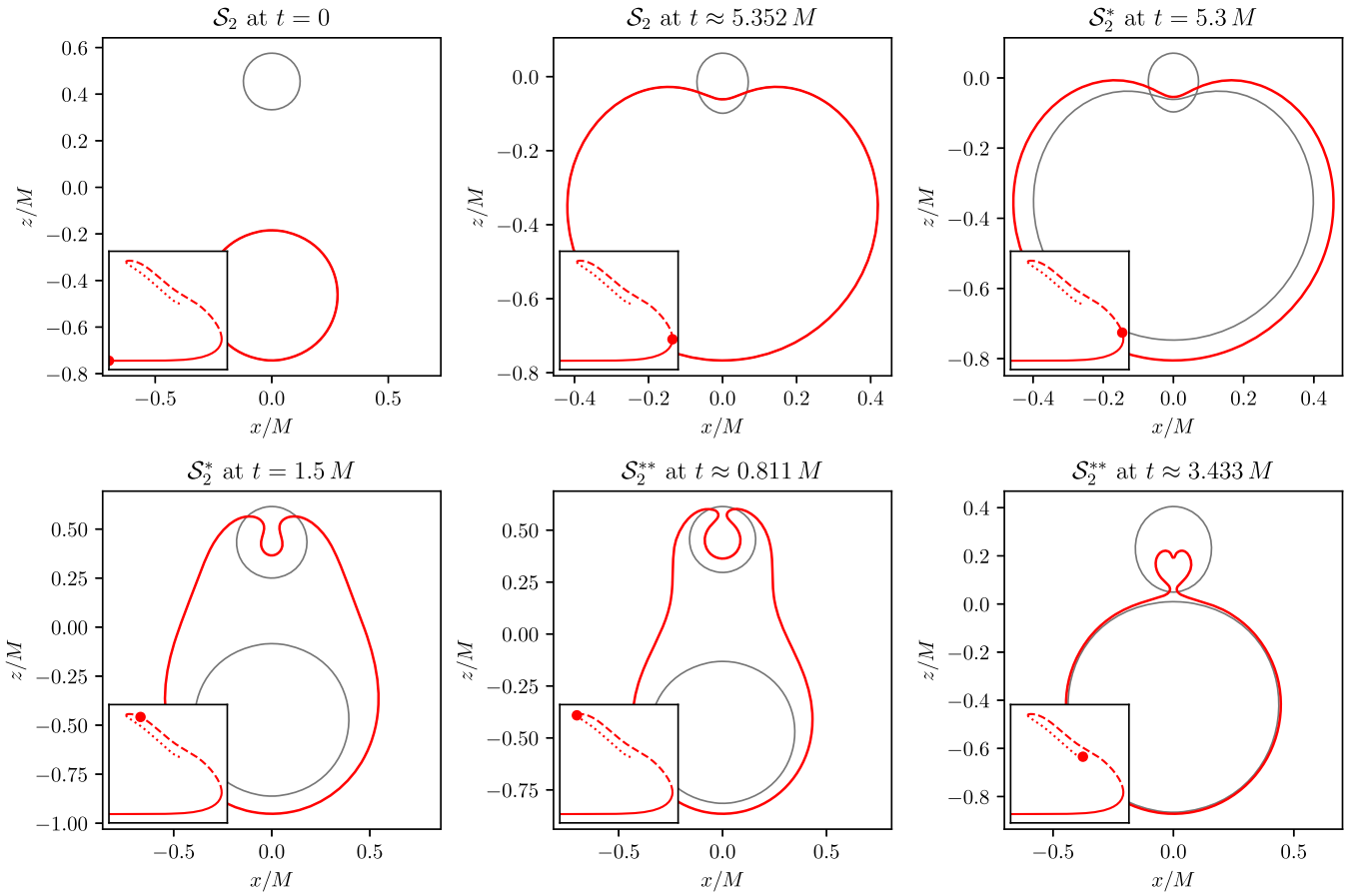

FIG. 5. Same as Fig. 4 but showing MOTSs along the connected MOTT consisting of $\mathcal{S}_2 \to \mathcal{S}_2^* \to \mathcal{S}_2^{**}$.

backwards until the point where it bifurcates with $\mathcal{S}_2^{**}$ at $t \approx 0.811M$ (bottom center panel). All MOTSs along this MOTT enclose only the puncture in the interior of $\mathcal{S}_2$, i.e., that of the larger of the two original black holes. The bottom right panel of Fig. 5 shows the last time we were able to reliably locate $\mathcal{S}_2^{**}$. Shortly after this time, it gets too close (in coordinates) to the puncture inside $\mathcal{S}_1$, resulting in loss of numerical accuracy. However, just as for $\mathcal{S}_{\text{inner}}$ and $\mathcal{S}_{\text{inner}}^{**}$, $\mathcal{S}_2^{**}$ approaches $\mathcal{S}_2$ from the outside. We suspect that $\mathcal{S}_2^{**}$ will subsequently move to the inside of $\mathcal{S}_2$ by forming a cusp at the time of transition. At this time, it must momentarily coincide with $\mathcal{S}_2$ in its lower portion and another MOTS ($\mathcal{S}_{1a}$, shown in Sec. IV C) in its upper portion. If true, this scenario would lead to a self-intersection forming in this world tube.

The annihilation of $\mathcal{S}_2$ with $\mathcal{S}_2^*$ resolves the previously unknown fate of this individual apparent horizon, although the fate of the full world tube (including $\mathcal{S}_2^*$ and $\mathcal{S}_2^{**}$) is not numerically resolved. We shall defer further discussion of possible scenarios to Sec. VII.

3. The world tube(s) of $\mathcal{S}_1$ and $\mathcal{S}_1^*$

At $t_{\text{bifurcate}}^{\mathcal{S}_1^*} \approx 0.756M$ we find the formation of the pair $(\mathcal{S}_1^*, \mathcal{S}_1^{**})$. These enclose the puncture inside $\mathcal{S}_1$ but do not contain the puncture of $\mathcal{S}_2$. Fig. 6 shows this pair along with $\mathcal{S}_1$ at a time $t = 2.5M$.

A merger and annihilation of $\mathcal{S}_1$ with $\mathcal{S}_1^*$ analogous to that of $\mathcal{S}_2$ with $\mathcal{S}_2^*$ could not be seen in this simulation.

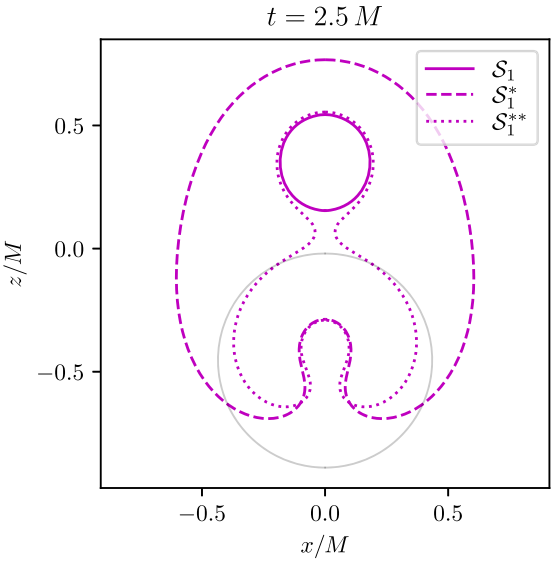

FIG. 6. Examples of the MOTSs $\mathcal{S}_1$, $\mathcal{S}_1^*$, and $\mathcal{S}_1^{**}$ at simulation time $t = 2.5M$. The light gray curve shows $\mathcal{S}_2$ for reference.

It is unclear if this lack of an annihilation is (a) purely due to the smaller $\mathcal{S}_1$ being closer in coordinates to one of the punctures, which increases the effect of the slow-down discussed above and in [59], or if (b) $\mathcal{S}_1$ has a qualitatively different behavior than $\mathcal{S}_2$ and possibly does not annihilate at all. One option to pursue the first possibility is to choose initial data for a simulation which reduces the aforementioned slow-down effects. Appendix B shows results for such a simulation, which suggests that the lack of annihilation could indeed be due to case (a) even in the present simulation.

Lastly, we would like to point out that, in a very similar way to $\mathcal{S}_2^{**}$, we find the inner branch $\mathcal{S}_1^{**}$ approaching one of the individual apparent horizons, this time $\mathcal{S}_1$, from the outside. In this case, however, we were able to resolve the formation of a cusp as $\mathcal{S}_1^{**}$ coincides with $\mathcal{S}_1 \cup \mathcal{S}_{2a}$ ($\mathcal{S}_{2a}$ is discussed in Sec. IV C). As expected, $\mathcal{S}_1^{**}$ subsequently self-intersects. This supports again the above expectation that this also happens for $\mathcal{S}_2^{**}$.

4. The world tube of $\mathcal{S}_0^*$

The last world tube is traced out by the pair $(\mathcal{S}_0^*, \mathcal{S}_0^{**})$, which bifurcates at $t_{\text{bifurcate}}^{\mathcal{S}_0^*} \approx 0.888M$. These do not connect smoothly to any of the above MOTSs. Figure 7 shows the MOTSs at a time $t = 2.5M$. None of the MOTSs along this world tube contain any puncture in their interior.

Based on the cases of cusp formation and self-intersections mentioned above, we speculate here on the future of $\mathcal{S}_0^{**}$ beyond the point where we are able to locate it reliably: We already mentioned the cusp formations of $\mathcal{S}_1^{**}$ and $\mathcal{S}_2^{**}$ in the previous two subsections. In these two cases, either $\mathcal{S}_1$ or $\mathcal{S}_2$ coincides with $\mathcal{S}_1^{**}$ or $\mathcal{S}_2^{**}$ on one of their portions, respectively. We also noted that in both cases the two remainders, $\mathcal{S}_{2a}$ and $\mathcal{S}_{1a}$, respectively, are themselves MOTSs discussed in Sec. IV C. These latter two MOTSs do not contain any puncture. They may, however, at some point touch and start to intersect, just like $\mathcal{S}_1$ and $\mathcal{S}_2$ do at t_{touch}. At the time when they touch, we propose that $\mathcal{S}_0^{**}$ coincides with their union, has a cusp at this time, and forms a self-intersection immediately afterwards. We are unfortunately not able to resolve this idea at this point since we lose numerical accuracy near the punctures before this can be observed.

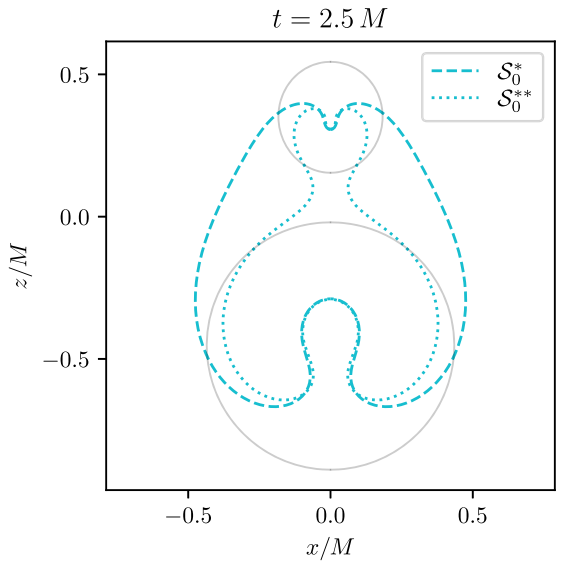

FIG. 7. Examples of the MOTSs $\mathcal{S}_0^*$ and $\mathcal{S}_0^{**}$ at simulation time $t = 2.5M$. The light gray curves show $\mathcal{S}_1$ and $\mathcal{S}_2$ for reference.

5. Comparison with the extreme mass ratio merger case

It is illuminating to compare these sequences of MOTSs to Fig. 16 in [35]. That paper studied marginally outer trapped open surfaces (MOTOSs) in Schwarzschild spacetimes with the argument that they could be used to model dynamical apparent horizon and other MOTT evolutions during an extreme mass ratio merger.

That paper did not include true dynamics, but it was argued that it should be possible to assemble the various MOTOSs found in Schwarzschild into a sequence describing the full dynamics of the merger. The authors proposed one such evolution, but what they did not consider[6] is that many of the steps could be happening simultaneously. Instead of creations and annihilations, they expected a single continuous sequence of MOTOSs evolving in time. If one reinterprets the sequence in their Fig. 16 as a marginally outer trapped open tube weaving backwards and forwards in time, then the proposed picture becomes much closer to that of Fig. 4 in the current paper, though still with some mistakes.

It is intriguing that simple model of an extreme mass ratio merger can reproduce cusp formation which subsequently evolves into self-intersections. However since [35] works with an exact solution, we can push further and see that this process may repeat indefinitely with surfaces involving more and more self-intersections. This then is extra evidence that the double self-intersection of Fig. 4 at $t \approx 4.967M$ is likely just the beginning of a sequence that may continue indefinitely with each n-times self-intersecting MOTOS ultimately being annihilating with an $(n+1)$-times self-intersecting MOTS which in turn was pair-created with a (soon-to-be) $(n+2)$-times self-intersecting MOTOS.

C. MOTSs inside $\mathcal{S}_1$ and $\mathcal{S}_2$

None of the MOTSs described thus far are located fully in the interior of either $\mathcal{S}_1$ or $\mathcal{S}_2$. As discussed in the first paper, we were in fact not able to locate such an interior MOTS in the Brill-Lindquist initial data. From the

[6]We are confident about this as two of them are also authors on the current paper!

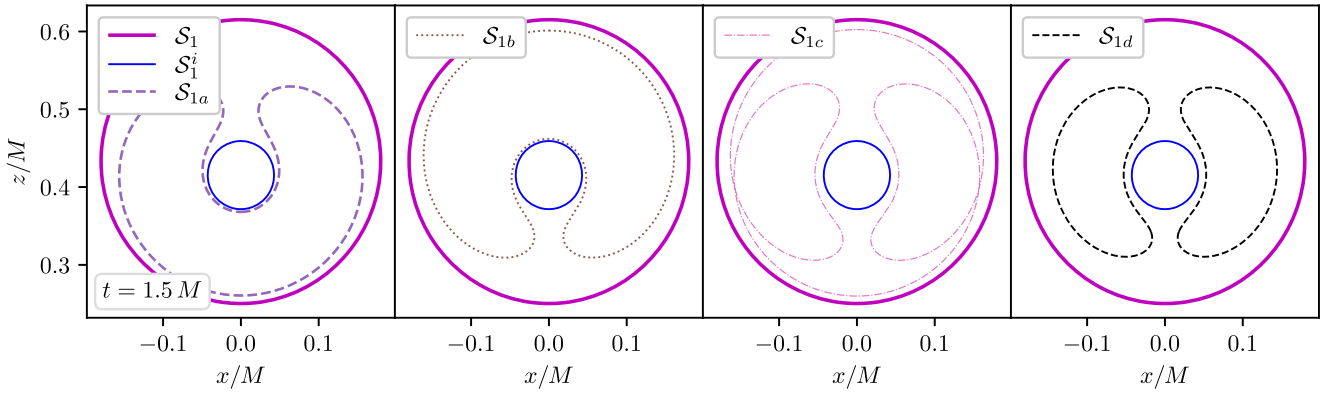

FIG. 8. The MOTSs $\mathcal{S}_{1a,b,c,d}$ in the interior of $\mathcal{S}_1$ at a simulation time $t = 1.5M$. $\mathcal{S}_{1a}$ (first panel) and $\mathcal{S}_{1b}$ (second panel) do not enclose the puncture inside $\mathcal{S}_1$, while $\mathcal{S}_{1c}$ (third panel) is self-intersecting and does enclose this puncture. The last panel shows a MOTS $\mathcal{S}_{1d}$ of toroidal topology. We also show a marginally *inner* trapped surface $\mathcal{S}_1^i$ as thin solid line, which is discussed in Sec. IV D.

discussion in the previous Sec. IV B, however, one would expect that at any point where a cusp forms in a MOTS, that MOTS coincides with the union of two other MOTSs as in the case of $\mathcal{S}_{\text{inner}}$ and $\mathcal{S}_1 \cup \mathcal{S}_2$ at t_{touch}. This holds for example for $\mathcal{S}^{**}_{\text{inner}}$ at the time it forms a cusp shortly before the last panel of Fig. 4. At that time, its lower portion coincides with $\mathcal{S}_2$ and the upper portion is fully contained inside $\mathcal{S}_1$. That is, at some point a MOTS must have formed inside $\mathcal{S}_1$ evolving into this self-intersecting shape. A similar argument holds for the lower portion of $\mathcal{S}_1^{**}$.

A search for MOTSs in the interior regions of $\mathcal{S}_1$ and $\mathcal{S}_2$ at a time $t > 0$ has indeed been successful. Figure 8 shows the four MOTSs we could locate inside $\mathcal{S}_1$ at a simulation time $t = 1.5M$. From Fig. 9 it can be seen that these MOTSs get closer (in coordinates) to $\mathcal{S}_1$ as $t \to 0$. The same qualitative behavior is found inside $\mathcal{S}_2$ and we will return to this point in Sec. IV D where we also discuss $\mathcal{S}_1^i$ and $\mathcal{S}_2^i$. Note that the self-intersecting MOTS $\mathcal{S}_{1c}$ later coincides with the upper portion of $\mathcal{S}^{**}_{\text{inner}}$ at the time the latter forms the cusp at $t \approx 4.32M$. Figure 10 shows this formation of a cusp and subsequent self-intersection. Similarly, $\mathcal{S}_{2a}$ coincides with the lower portion of $\mathcal{S}_1^{**}$ as it forms its cusp at about $t \approx 4.9M$. Another observation is that these interior MOTSs cannot "escape" their enclosing $\mathcal{S}_1$ or $\mathcal{S}_2$, respectively, while the latter exist. This is again easily explained by the maximum principle for MOTSs given in Section 3.2 of Ref. [21], since any common point

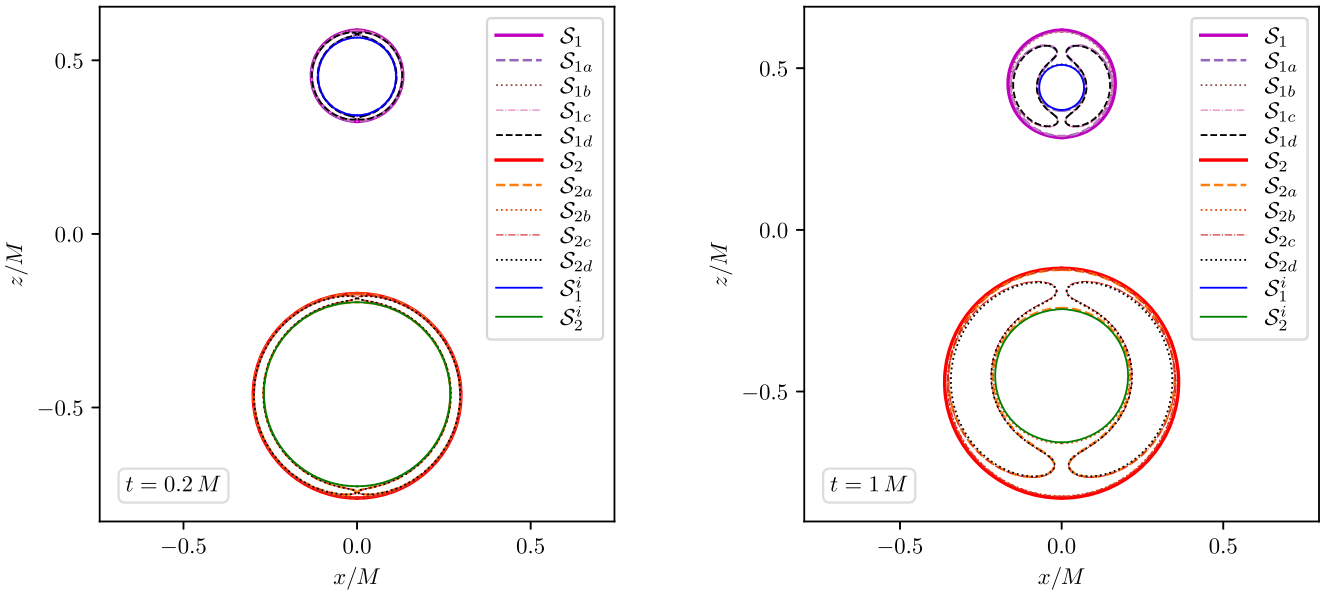

FIG. 9. MOTSs in the interior of the individual MOTSs $\mathcal{S}_1$ and $\mathcal{S}_2$ at the two different times $t = 0.2M$ (left panel) and $t = 1M$ (right panel). Any MOTS outside or partially outside the individual ones is not shown here. The MOTSs $\mathcal{S}_{1a,b,c,d}$ are shown individually in Fig. 8. We furthermore show the MITSs $\mathcal{S}_1^i$, $\mathcal{S}_2^i$, which are discussed in Sec. IV D.

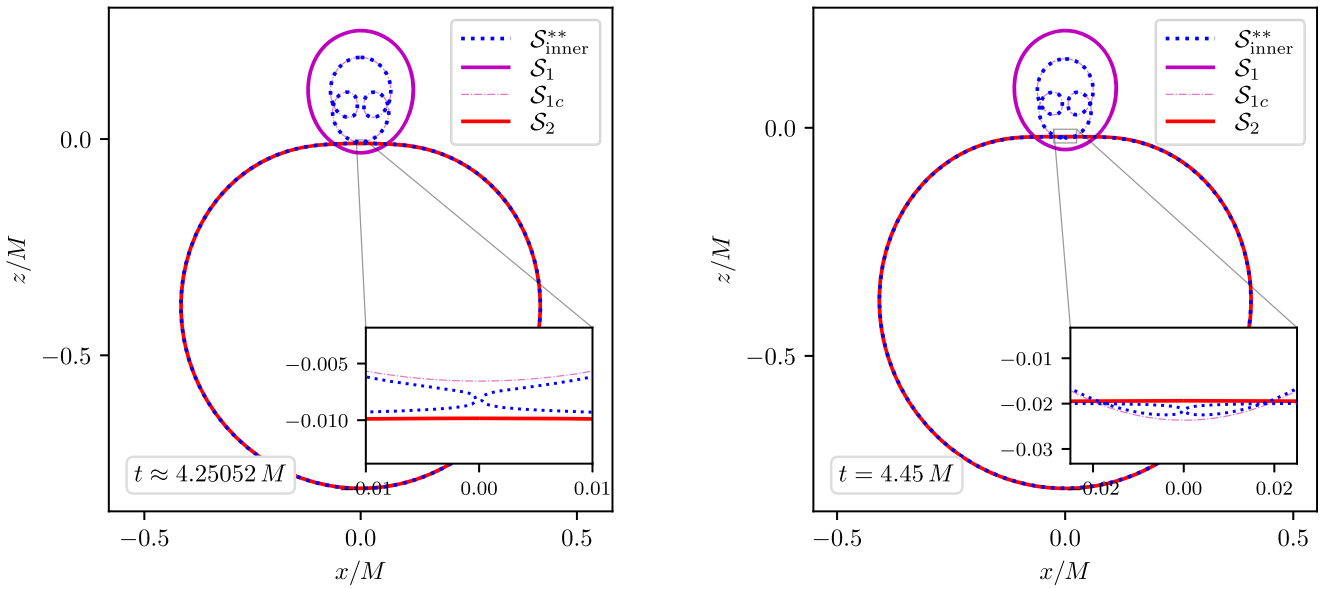

FIG. 10. Cusp formation with subsequent self-intersection in the evolution of $\mathcal{S}^{**}_{\text{inner}}$. The left panel shows a time before cusp formation and the right panel a time after. Note that the cusp forms at the time when $\mathcal{S}_{1c}$ and $\mathcal{S}_2$ touch. At that time, $\mathcal{S}^{**}_{\text{inner}}$ coincides with the union $\mathcal{S}_{1c} \cup \mathcal{S}_2$. The interior self-intersecting MOTSs are very similar to those seen in pure Schwarzschild in [35].

with a common normal direction would imply the MOTSs necessarily coincide.

Interestingly, $\mathcal{S}_{1d}$ and $\mathcal{S}_{2d}$ are MOTSs with toroidal topology, i.e., their Euler characteristic is $\chi = 0$ in contrast to all other MOTSs which have $\chi = 2$. We numerically verified that their shear σ^+_{AB} does not vanish, which immediately implies that any first order spacelike outward deformation does not lead to an untrapped surface (see the remark at the end of Sec. III A of Ref. [16]). This is compatible with a negative principal eigenvalue of the stability operator, which we find as well. $\mathcal{S}_{1d}$ is shown in the last panel of Fig. 8 and closely follows the loop of the self-intersecting $\mathcal{S}_{1c}$.

All these interior MOTSs get very close in coordinates to one of the punctures and we hence lose most of them due to numerical problems before the end of our simulation. This happens earlier for $\mathcal{S}_{1a,b,c,d}$ than for $\mathcal{S}_{2a,b,c,d}$ as the former are smaller in coordinates than the latter.

D. MOTSs seen from the other asymptotic ends

Figures 8 and 9 show curves $\mathcal{S}^i_1$ and $\mathcal{S}^i_2$ which we did not yet comment on. These curves belong to marginally *inner* trapped surfaces (MITSs), where $\Theta_- = 0$ with no condition on Θ_+. Equivalently, these surfaces are MOTSs with the notion of *inward* and *outward* reversed. These MITSs are interesting for several reasons.

First, the MITSs provide a means for generalizing a feature visible in the time-symmetric case (see paper I), where the MOTSs with sharp turns seem to transition between portions staying close to one of the other MOTSs with fewer or no turns. However, at these turns the notion of inside and outside may switch. This is irrelevant in time-symmetry as in that case $\Theta_+ = 0 \Leftrightarrow \Theta_- = 0$, but it becomes important during the simulation where time-symmetry is lost. As can be seen in Fig. 8, the MOTSs $\mathcal{S}_{1a,b,c,d}$ run close to $\mathcal{S}^i_1$ on an extended portion, consistent with the notions of inside and outside there. Figure 11 visualizes this idea by showing the spatial part of the respective null normals with vanishing expansion, i.e., of ℓ^+ for the MOTSs and ℓ^- for the MITS. We find that all

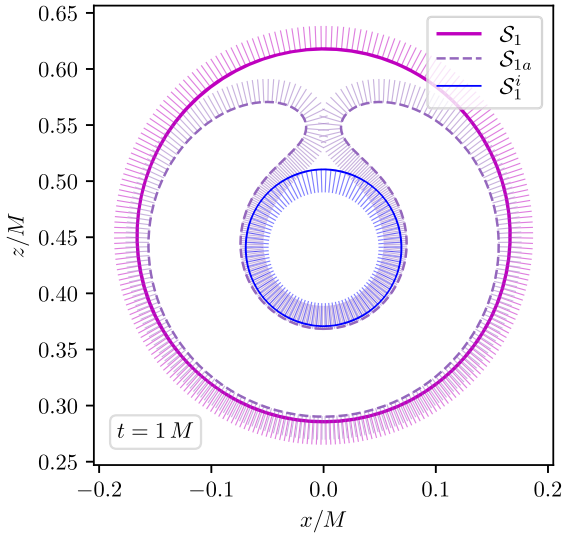

FIG. 11. Spatial outward normal directions on $\mathcal{S}_1$ and one of the interior MOTSs $\mathcal{S}_{1a}$ as well as the inward normal direction on the MITS $\mathcal{S}^i_1$.

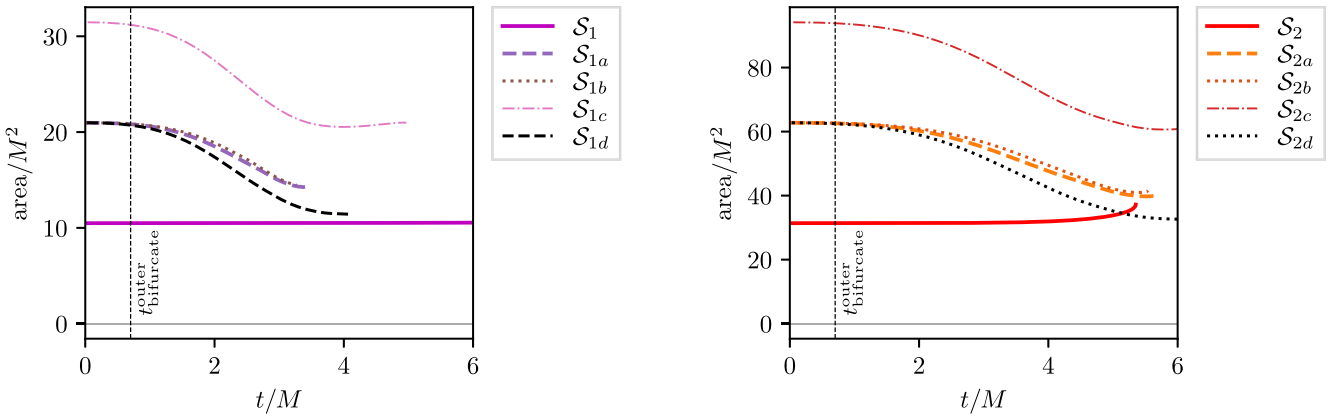

FIG. 12. Evolution of the area of the MOTSs $\mathcal{S}_{1a,b,c}$ inside $\mathcal{S}_1$ (left panel) and of $\mathcal{S}_{2a,b,c}$ inside $\mathcal{S}_2$ (right panel). The areas of $\mathcal{S}_1$ and $\mathcal{S}_2$ are shown for reference. Note that the smooth annihilation of $\mathcal{S}_2$ is not visible since we do not include the area of the connecting MOTS $\mathcal{S}^*_2$.

MOTSs in the interior of $\mathcal{S}_1$ fully lie in the annular region between $\mathcal{S}_1$ and the MITS $\mathcal{S}^i_1$. The MOTSs in the interior of $\mathcal{S}_2$ behave analogously.

This also allows us to explain the behavior of the interior MOTSs $\mathcal{S}_{1a,b,c,d}$ and $\mathcal{S}_{2a,b,c,d}$ for $t \to 0$. In this limit, $\mathcal{S}^i_{1,2}$ coincide with $\mathcal{S}_{1,2}$, respectively, and so, being confined between these, the interior MOTSs do as well. From this behavior and the number of turns in their shapes, one may expect that for $t \to 0$ the area of $\mathcal{S}_{1a,b}$ and $\mathcal{S}_{1d}$ becomes twice the area of $\mathcal{S}_1$ while $\mathcal{S}_{1c}$ should have three times this area. Analogous arguments hold for $\mathcal{S}_{2a,b,c,d}$. Figure 12 confirms this expectation and shows the evolution of the various areas as a function of time.

Another reason to consider MITSs is that the two punctures in the Brill-Lindquist initial data belong to two different asymptotically flat ends of the slice Σ. In fact, these data contain three ends with $x \to \infty$ representing the end we commonly choose to be in the "outward" direction. The ends $x \to x_1$ and $x \to x_2$, where $x_{1,2}$ are the coordinates of the two punctures, contain equally valid observers far away from any black hole. An observer near x_1 or x_2 will see a quite different picture of what "we" (i.e., observers for whom $x \to \infty$ is considered outside) see as a binary black hole merger. In particular, at $t = 0$ where $\mathcal{S}_{1,2}$ are not only MOTSs but also MITSs, an observer near, say, x_1 interprets $\mathcal{S}_1 = \mathcal{S}^i_1$ as *common* apparent horizon enclosing both punctures. Figure 13 shows that the area of these MITSs is monotonically increasing. Furthermore, considered as MOTSs seen from the respective asymptotic region, $\mathcal{S}^i_1$ and $\mathcal{S}^i_2$ are strictly stable and, in fact, the *outermost* common MOTSs representing a perturbed Schwarzschild black hole.

It is therefore clear why we cannot find any of the interior MOTSs inside $\mathcal{S}_{1,2}$ in the time-symmetric initial slice. That slice continues from the respective MOTSs $\mathcal{S}_{1,2}$ directly to the "outside" of the apparent horizons $\mathcal{S}^i_{1,2}$ seen from the other asymptotic regions. At later times, however, the slice does contain a nonvanishing volume between $\mathcal{S}^i_{1,2}$ and $\mathcal{S}_{1,2}$, respectively, where the additional MOTSs are located. It is noteworthy that an analogous region of the Schwarzschild spacetime is contained in a slice in Painlevé-Gullstrand coordinates, where self-intersecting MOTSs were found in Ref. [35].

While many more MITSs are likely present in our simulations, we shall leave a more exhaustive study of these surfaces for future work.

E. Remarks on initial distance and mass ratio

Most of the discussed numerical results are obtained from simulations starting with a single physical configuration, namely Brill-Lindquist initial data consisting of a conformally flat three-metric with conformal factor (21) where the bare masses are $m_1 = 1/3$ and $m_2 = 2/3$ and the distance parameter is chosen as $d = 0.9$. This choice balances several effects resulting from the interplay of the employed slicing and the numerical setup: A larger value for d makes the individual apparent horizons $\mathcal{S}_{1,2}$

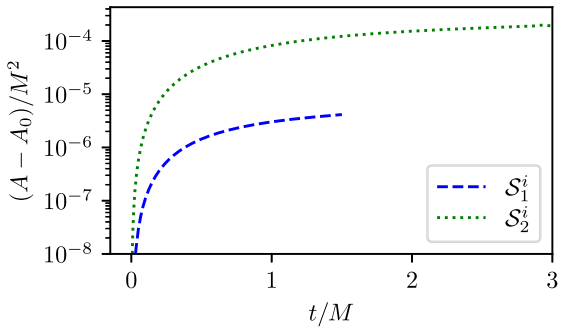

FIG. 13. Evolution of the area of the MITSs $\mathcal{S}^i_1$ and $\mathcal{S}^i_2$. We plot the difference $A - A_0$ on a logarithmic scale to emphasize the area change. Here A_0 is the area of the MITS at $t = 0$ where it coincides with the area of $\mathcal{S}_1$ and $\mathcal{S}_2$, respectively.

slow down in evolution before they start to intersect [59] and thus prevents us from observing the annihilations of $(\mathcal{S}_2, \mathcal{S}_2^*)$ and $(\mathcal{S}_{\text{inner}}, \mathcal{S}_{\text{inner}}^*)$. A smaller value leads to common MOTSs $\mathcal{S}_{\text{outer}}$ and $\mathcal{S}_{\text{inner}}$ already being present in the initial data. As shown in paper I, many more common MOTSs exist in these kinds of setups and hence at least some of the various bifurcations do not exist in the simulation.

Similar considerations led to the chosen mass ratio of $q = 2$. In particular, it is true that more unequal masses keep the larger MOTS $\mathcal{S}_2$ further away (in coordinates) from the puncture in its interior. As a consequence, it suffers less from the slow-down described in [59] and we can observe that it annihilates with $\mathcal{S}_2^*$ "earlier" with respect to simulation time. However, this comes at the cost of $\mathcal{S}_2^*$ now getting too close (again, in coordinates) to the puncture inside the *smaller* MOTS $\mathcal{S}_1$ and thus we were not able to resolve the full world tube of $\mathcal{S}_2^*$ and show that it turns around in time at *both* of its ends. This also means that the prospect of resolving the fate of $\mathcal{S}_1$ crucially depends on keeping it as far away from its puncture as possible. Without modifying the used gauge conditions, which we do not try to do in the present work, this can only be achieved with more equal masses. Our attempts to do so are summarized in Appendix B. However, we find that this requires a very small initial distance d.

Thus, while we are indeed able to resolve some of the previously presented features for many choices of initial data, the particular choice we made combines most of these in one simulation. Furthermore, the reasons we cannot resolve the full set of these features for other mass ratios or initial distances are well understood and due to numerical issues. We therefore have no clear indication that the observed behavior should indeed be specific to our choice of these parameters. The exception is a possible qualitative change in case of a large mass ratio. For large q, we find that the time $t^{\mathcal{S}_2}_{\text{annihilate}}$ where $\mathcal{S}_2$ annihilates with $\mathcal{S}_2^*$ occurs earlier and much closer to the time t_{touch} when $\mathcal{S}_1$ and $\mathcal{S}_2$ start to intersect. Recall that t_{touch} is precisely the time when the union $\mathcal{S}_1 \cup \mathcal{S}_2$ coincides with $\mathcal{S}_{\text{inner}}$ and that this provides the connection between $\mathcal{S}_{1,2}$ and $\mathcal{S}_{\text{outer}}$ [25,26]. We have verified for $d = 0.9$ that $t_{\text{touch}} < t^{\mathcal{S}_2}_{\text{annihilate}}$ up to $q = 14$. However, if one finds for even larger q that $\mathcal{S}_2$ annihilates with $\mathcal{S}_2^*$ before it intersects with $\mathcal{S}_1$, one may still be able to find a sequence of MOTSs connecting $\mathcal{S}_{1,2}$ with $\mathcal{S}_{\text{outer}}$. In this case, the connection may occur after $\mathcal{S}_2$ has turned around in time, i.e., one may see a coincidence of $\mathcal{S}_1 \cup \mathcal{S}_2^*$ with $\mathcal{S}_{\text{inner}}^*$.

V. STABILITY

The various bifurcations and annihilations described thus far can also be understood with the help of the MOTS stability operator. As we shall see, this not only gives strong numerical support for our claims of smooth bifurcations and annihilations, it also provides a useful characterization of the respective two branches in terms of the eigenvalues of this operator.

Let L_Σ be the stability operator (12). As shown in Proposition 5.1 of [32], the vanishing of the principal eigenvalue of L_Σ is closely related to bifurcations and annihilations of a MOTS. The intuitive picture is that of a MOTT $\mathcal{H}$ which is tangent to one of the slices Σ_{t^*}, where t^* is the time of bifurcation or annihilation. At this time, the cross section $\mathcal{S}_{t^*}$ of $\mathcal{H}$ is a MOTS with vanishing principal eigenvalue $\lambda_0 = 0$. Essentially, the proposition proves, under suitable genericity conditions satisfied in all our cases, that the existence of such a MOTS $\mathcal{S}_{t^*}$ with $\lambda_0 = 0$ implies for a given foliation of spacetime the existence of a *unique* MOTT $\mathcal{H}$ compatible with that foliation and containing $\mathcal{S}_{t^*}$. That MOTT is necessarily tangent to Σ_{t^*}. Hence, if we do find two MOTTs connecting smoothly at t^* with $\lambda_0 \to 0$ as $t \to t^*$, then we have a clear numerical indication for such a bifurcation or annihilation. This is precisely the case for the bifurcation of the pair $(\mathcal{S}_{\text{outer}}, \mathcal{S}_{\text{inner}})$ and the annihilation of the pair $(\mathcal{S}_2, \mathcal{S}_2^*)$ shown in Figs. 14 and 15. However, for the other pairs of MOTSs, we in fact find that instead of the principal eigenvalue, it is one of the *higher* eigenvalues which tends to zero at bifurcation or annihilation time.

An interesting observation we can make here is that the number of negative eigenvalues necessarily changes as we follow a smooth MOTT across such a bifurcation or annihilation. Three of the MOTSs, namely $\mathcal{S}_{\text{outer}}$, $\mathcal{S}_1$, and $\mathcal{S}_2$, possess a positive principle eigenvalue, i.e., they are strictly stable and thus act as barrier for trapped and untrapped surfaces in a neighborhood. By our terminology, they are apparent horizons and the world tubes they trace out are dynamical apparent horizons. The above

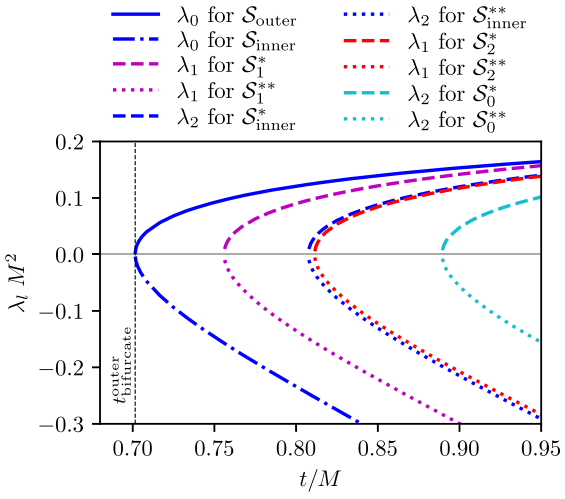

FIG. 14. Eigenvalues of L_Σ for the ten MOTSs participating in the five bifurcations. For each MOTS, we show the respective eigenvalue which tends to zero as $t \to t_{\text{bifurcate}}$.

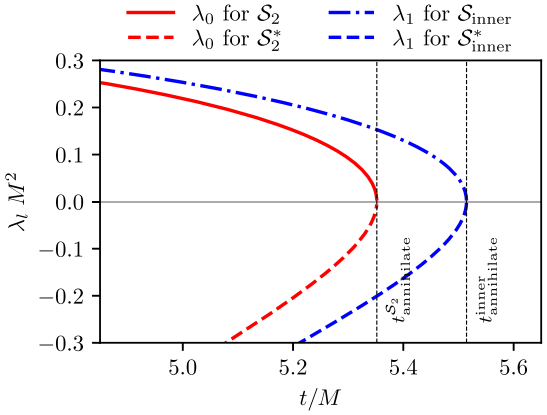

FIG. 15. Eigenvalues of L_Σ for the two pairs of MOTSs $(\mathcal{S}_2, \mathcal{S}_2^*)$ and $(\mathcal{S}_{\rm inner}, \mathcal{S}^*_{\rm inner})$ close to the time when they annihilate.

properties are what one would usually expect from horizons associated with black holes. All other MOTSs we found possess one or more negative eigenvalues. At any given time, all MOTSs with a negative eigenvalue are contained in the interior of one of the strictly stable ones, i.e., $\mathcal{S}_1$, $\mathcal{S}_2$, or $\mathcal{S}_{\rm outer}$. To present our results more systematically, let N_- be the number of eigenvalues $\lambda_{l,m} < 0$ and N^0_- the number of eigenvalues $\lambda_{l,m=0} < 0$. Table I lists the various values of N_- and N^0_- we find for the MOTSs along each MOTT during the evolution and Fig. 16 shows all MOTSs at two different times with N^0_- indicated by line thickness and color. In each instance where a MOTS transitions through a bifurcation or annihilation along the indicated sequences of MOTTs, one additional negative eigenvalue of the $m = 0$ mode appears.

Another observation is related to the instances where two MOTSs touch at one point and coincide at this time with a MOTS having a cusp. We were able to explicitly resolve three of these coincidences numerically, namely $\mathcal{S}_1 \cup \mathcal{S}_2 = \mathcal{S}_{\rm inner}$, $\mathcal{S}_{1c} \cup \mathcal{S}_2 = \mathcal{S}^{**}_{\rm inner}$ and $\mathcal{S}_1 \cup \mathcal{S}_{2a} = \mathcal{S}^{**}_1$. Based on our results, we expect at least two more such coincidences, which we could not resolve for numerical reasons. These are $\mathcal{S}_{1a} \cup \mathcal{S}_2 = \mathcal{S}^{**}_2$ and $\mathcal{S}_{1a} \cup \mathcal{S}_{2a} = \mathcal{S}^{**}_0$. For all these cases where $\mathcal{S} \cup \mathcal{S}' = \mathcal{S}''$, we find, with obvious notation, that

$$N^0_- + N^{0\prime}_- + 1 = N^{0\prime\prime}_-. \tag{22}$$

Note that N^0_- is constant along each individual MOTT, even when cusps and self-intersections form, as they do for $\mathcal{S}_{\rm inner}$, $\mathcal{S}^{**}_{\rm inner}$ and $\mathcal{S}^{**}_1$. However, in several instances, we find that eigenvalues of the higher angular modes ($m \neq 0$) do cross zero on perfectly smooth portions of the MOTT. Due to the axisymmetry and absence of spin in our simulation, we have a $\pm m$ degeneracy in the spectrum, whence all zero crossings of eigenvalues $\lambda_{l,m\neq 0}$ happen in multiples of 2. Two examples of such cases are depicted in Fig. 17, which

TABLE I. Number of negative eigenvalues of L_Σ for the MOTSs along the different MOTTs. The arrows indicate when we have found a smooth connection between the respective world tubes, while the arrow in parentheses indicates a suspected smooth transition which we could not resolve numerically. Shown is N^0_-, i.e., the number of eigenvalues $\lambda_{l,m=0} < 0$ as well as N_- for the number of all negative eigenvalues. This latter value changes for some of the MOTTs, in which case we list all the occurring cases (not in order of appearance).

MOTT	$\mathcal{H}_1$ $(\rightarrow)$	$\mathcal{H}^*_1$ $\rightarrow$	$\mathcal{H}^{**}_1$	
N^0_-	0	1	2	
N_-	0	1	2, 4	
MOTT	$\mathcal{H}_2$ $\rightarrow$	$\mathcal{H}^*_2$ $\rightarrow$	$\mathcal{H}^{**}_2$	
N^0_-	0	1	2	
N_-	0	1	2, 4	
MOTT	$\mathcal{H}_{\rm outer}$ $\rightarrow$	$\mathcal{H}_{\rm inner}$ $\rightarrow$	$\mathcal{H}^*_{\rm inner}$ $\rightarrow$	$\mathcal{H}^{**}_{\rm inner}$
N^0_-	0	1	2	3
N_-	0	1, 3	2, 4	3, 5, 7, 9
MOTT			$\mathcal{H}^*_0$	$\mathcal{H}^{**}_0$
N^0_-			2	3
N_-			2	3, 5, 7
MOTT	$\mathcal{H}_{1a}$	$\mathcal{H}_{1b}$	$\mathcal{H}_{1c}$	$\mathcal{H}_{1d}$
N^0_-	1	1	2	2
N_-	3	1, 3	4, 6	4, 6
MOTT	$\mathcal{H}_{2a}$	$\mathcal{H}_{2b}$	$\mathcal{H}_{2c}$	$\mathcal{H}_{2d}$
N^0_-	1	1	2	2
N_-	1, 3	1	4	4

shows that the two degenerate eigenvalues $\lambda_{1,\pm 1}$ of $\mathcal{S}^{**}_2$ and $\mathcal{S}^{**}_1$ do cross zero during their evolution. This crossing happens twice for the latter case. Taking invertibility of L_Σ as indicator for the existence of a smooth evolution of a MOTS $\mathcal{S}$, we here have explicit counterexamples showing that the converse of this statement is not true. In other words, invertibility of L_Σ is only a sufficient but not a necessary condition for a smooth evolution.

VI. SIGNATURE AND INGOING EXPANSION

As discussed in Sec. II B 2, a strictly stable MOTS, $\lambda_0 > 0$, belongs to a dynamical apparent horizon that has spacelike signature at that point (cf. [17,18]). Together with $\Theta_- \leq 0$, the area will be nondecreasing. Since we see in Fig. 3 that many of the MOTSs have a decreasing or nonmonotonic area evolution, we expect that those with $\lambda_0 < 0$ cannot have both nonpositive ingoing expansion $\Theta_- \leq 0$ and evolve along a spacelike MOTT. Examples are shown in Figs. 18 and 19 where we see complicated signature changes and indefiniteness of the sign of Θ_- along the world tubes $\mathcal{H}_{\rm inner}$ and $\mathcal{H}^*_{\rm inner}$. In these figures, time increases upwards and the signature or sign of Θ_- is shown as color on the world tubes. Figure 20 shows a close-up of the sign of Θ_- at the top end where $\mathcal{S}_{\rm inner}$ and $\mathcal{S}^*_{\rm inner}$

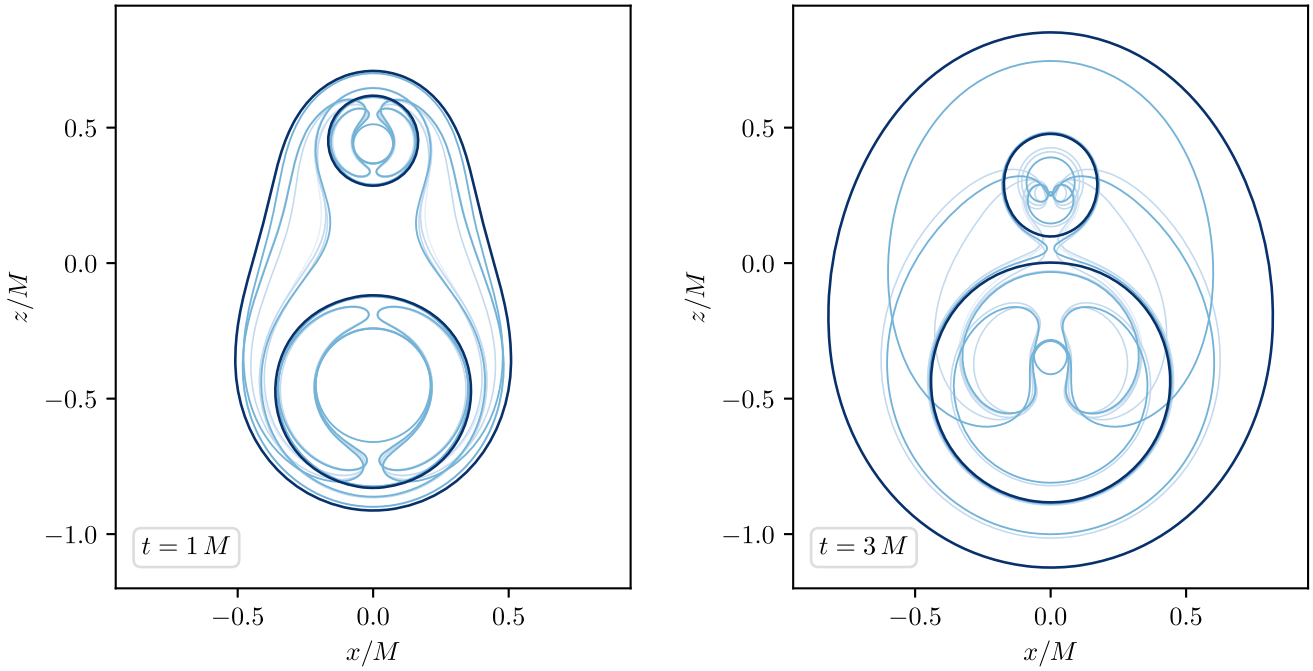

FIG. 16. MOTSs at two different times of the simulation. The line thickness and color reflects N^0_-, i.e., the number of negative stability eigenvalues of the $m = 0$ mode. The three dark lines in both panels are $\mathcal{S}_{\text{outer}}$ (common), $\mathcal{S}_1$ (upper) and $\mathcal{S}_2$ (lower). Lighter colors show MOTSs with larger N^0_-. Note that none of the MOTSs extends beyond $\mathcal{S}_{\text{outer}}$.

annihilate (or equivalently where $\mathcal{H}_{\text{inner}}$ and $\mathcal{H}^*_{\text{inner}}$ connect smoothly). A qualitatively very similar behavior of these quantities is found for all MOTTs except $\mathcal{H}_{\text{outer}}$, $\mathcal{H}_1$ and $\mathcal{H}_2$. These are purely spacelike and have $\Theta_- \leq 0$ at most times.[7]

A result of Bousso and Engelhardt [39,63] shows that even when $\mathcal{H}$ changes direction in time and has nonspacelike segments, it will have a monotonic area evolution provided several conditions hold on $\mathcal{H}$. One of these is that $\Theta_- \leq 0$, which we have already seen to not be satisfied for most MOTTs we found in this simulation. At this point, one could immediately conclude that this result is not applicable to most of our cases and hence finding nonmonotonic area evolutions is not in tension with any theoretical expectation. While certainly true, we still think it is worthwhile to show which of the other assumptions made in the proof are violated, not least because they were believed to be unrestrictive.

To state the relevant ones here, we go back to the evolution vector $\mathcal{V}^\alpha$ defined as tangent to $\mathcal{H}$ and orthogonal to each MOTS $\mathcal{S}$ foliating $\mathcal{H}$. As before, we fix its scaling by requiring $\mathcal{L}_\mathcal{V} t = 1$. Since the null normals $\ell^\pm$ span the two-dimensional space of normals to $\mathcal{S}$, we can write

$$\mathcal{V}^\alpha = b\ell^\alpha_+ + c\ell^\alpha_-. \tag{23}$$

As $\mathcal{V}\cdot\mathcal{V} = -2bc$, the coefficients b and c are related to the signature of $\mathcal{H}$, i.e., $\mathcal{H}$ is spacelike, timelike, or null when $bc < 0$, $bc > 0$, or $bc = 0$, respectively. The proof in [63]

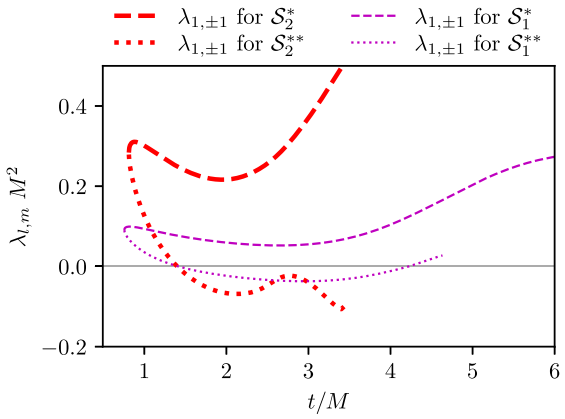

FIG. 17. Examples of eigenvalues with $m \neq 0$ crossing zero on the smoothly evolving portions of $\mathcal{S}_2^{**}$ (thick dotted line) and $\mathcal{S}_1^{**}$ (thin dotted line). The smoothly connecting respective curves for $\mathcal{S}_2^*$ and $\mathcal{S}_1^*$ are added here for reference. Note that both $\mathcal{S}_2^{**}$ and $\mathcal{S}_1^{**}$ have a principal eigenvalue $\lambda_0 < 0$ and $\lambda_{1,0} < 0$, which are not shown.

[7]We do find a very short duration of $\Delta t \approx 0.04M$ after $t^{\text{outer}}_{\text{bifurcate}}$ where $\mathcal{S}_{\text{outer}}$ has a small portion with $\Theta_- > 0$ close to its equator. This was also found in [28]. A similar portion with $\Theta_- > 0$ is found on $\mathcal{S}_2$ shortly ($\Delta t \approx 0.02M$) before it annihilates with $\mathcal{S}_2^*$. Both of these portions smoothly connect with corresponding portions on the MOTSs they connect to ($\mathcal{S}_{\text{inner}}$ for $\mathcal{S}_{\text{outer}}$ and $\mathcal{S}_2^*$ for $\mathcal{S}_2$).

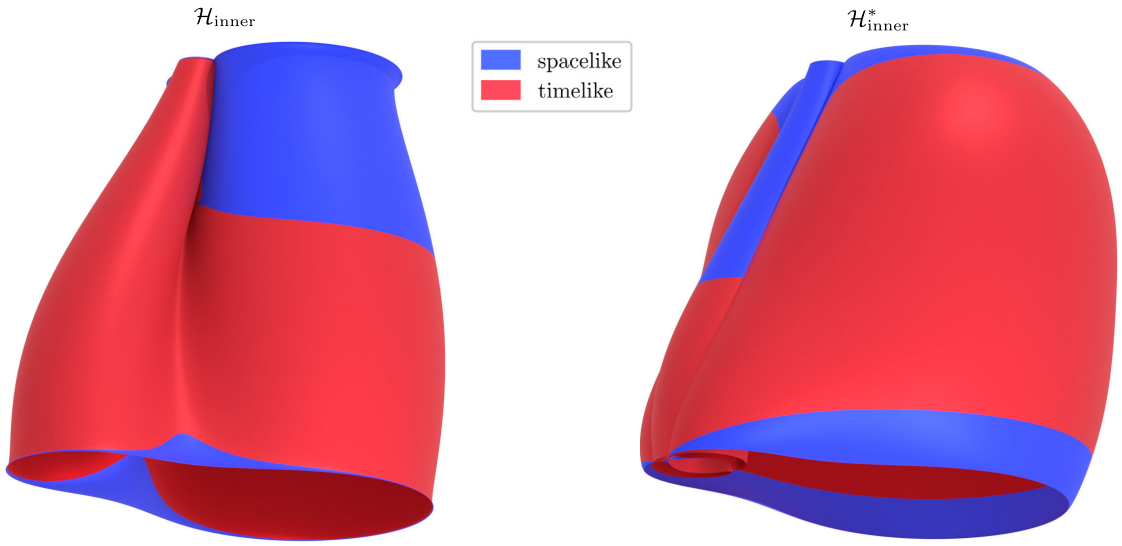

FIG. 18. Signature of $\mathcal{H}_{\text{inner}}$ (left panel) and $\mathcal{H}^*_{\text{inner}}$ (right panel). In these tube plots, time goes upwards and z-values increase to the left. These two MOTTs smoothly connect at their top ends but not at the bottom as they connect with different world tubes there. The bottom end of the right panel corresponds to the bottom-left panel of Fig. 4.

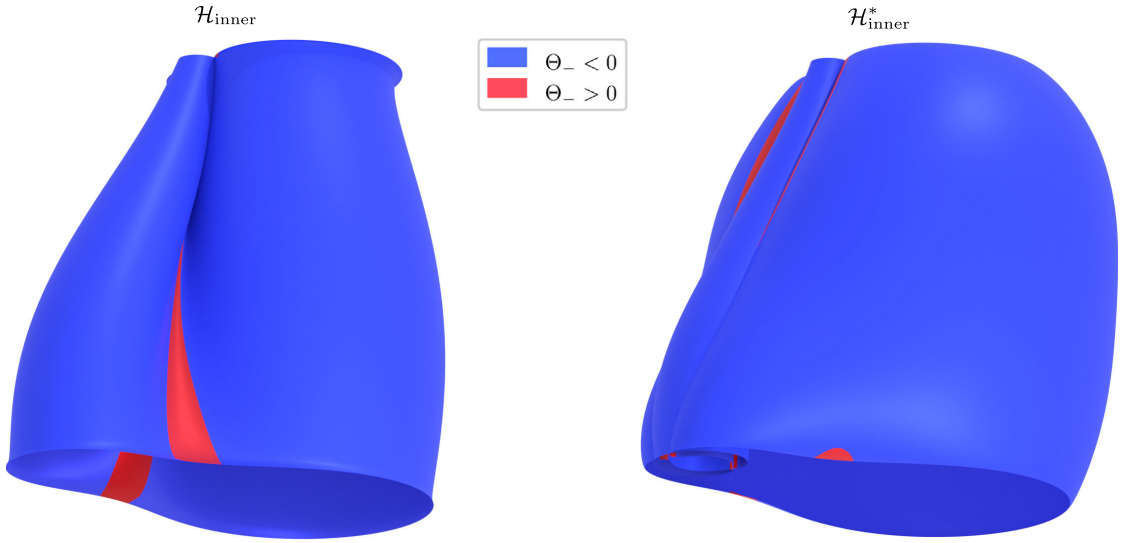

FIG. 19. Sign of the ingoing expansion Θ_- of $\mathcal{S}_{\text{inner}}$ (left panel) and $\mathcal{S}^*_{\text{inner}}$ (right panel) plotted on their respective MOTTs $\mathcal{H}_{\text{inner}}$ and $\mathcal{H}^*_{\text{inner}}$ in the same perspective as in Fig. 18. The portion with $\Theta_- > 0$ of $\mathcal{S}_{\text{inner}}$ (left panel) smoothly connects to a corresponding portion on $\mathcal{S}_{\text{outer}}$, which quickly vanishes after $\Delta t \approx 0.04M$ (not shown here).

now requires in addition to genericity assumptions satisfied in all our cases, the following:

(i) Every inextendible portion of definite sign of c is entirely timelike or contains at least one full MOTS.
(ii) Every MOTS in $\mathcal{H}$ splits a Cauchy slice Σ that it is contained in into two disjoint portions.

Then, without restrictions on Θ_-, it is proven that c cannot change sign on $\mathcal{H}$. On all but the three strictly stable MOTTs, however, we find that at least one of the above conditions is violated and that, in fact, both b and c do change sign.

In cases of self-intersections, it is clearly condition (ii) that does not hold. But even for MOTSs that do not self-intersect (or on portions of their world tubes on which they do not self-intersect), we find that condition (i) is violated. For the case of $\mathcal{S}_{\text{inner}}$, this was discussed in great detail in [27]. With the annihilation of $\mathcal{S}_{\text{inner}}$ with $\mathcal{S}^*_{\text{inner}}$, we are now able to extend these results to later times.

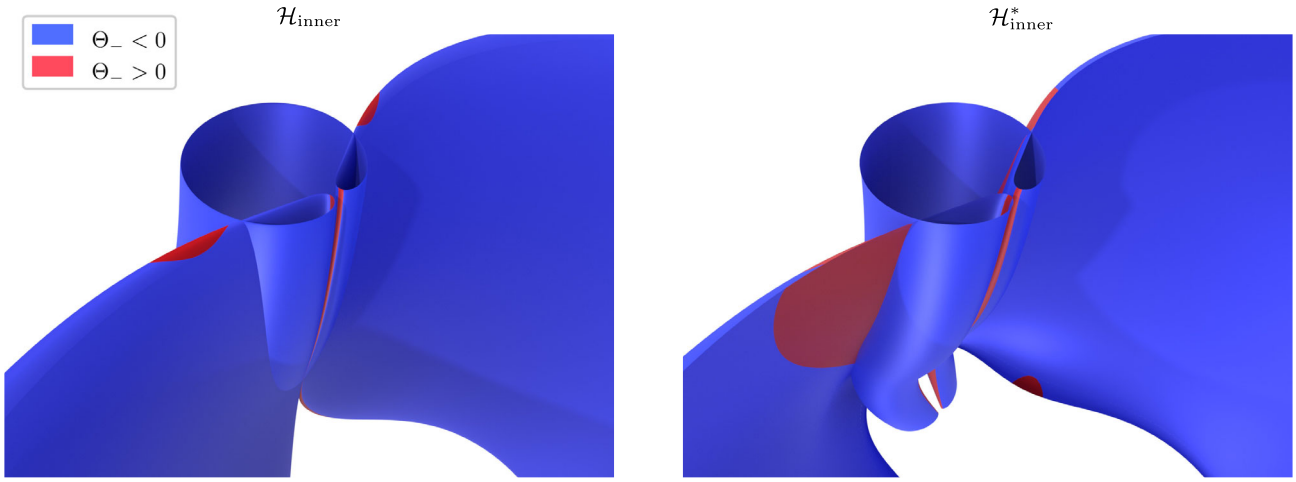

FIG. 20. Close-up of the top ends of the MOTTs shown in Fig. 19. The two world tubes smoothly join at this top end and the portions with $\Theta_- < 0$ connect across this annihilation.

In particular, shortly before $\mathcal{S}_{\text{inner}}$ vanishes, its world tube $\mathcal{H}_{\text{inner}}$ becomes purely spacelike with $c < 0$ on full MOTSs. At these times, however, $\mathcal{S}_{\text{inner}}$ has self-intersections, i.e., this presents an explicit example that (i) is not a sufficient condition.

VII. CONCLUSIONS

In the present second paper of this two-part study, the new generalized shooting method introduced in the first paper was used successfully to uncover new MOTSs forming during the head-on merger of two nonspinning black holes, including MOTSs of toroidal topology. This has vastly increased the number and variety of known MOTSs and also shows that they can have a much richer range of geometrical properties than had been previously expected.

However this increase has also highlighted the rarity and significance of stable MOTSs. Only three out of all the multitude that we have observed are stable—even strictly stable except for the points of annihilation or bifurcation—and trace out spacelike world tubes. These are exactly the MOTSs that one would naturally associate with black hole boundaries: the two individual black holes ($\mathcal{S}_1$ and $\mathcal{S}_2$) and the final remnant ($\mathcal{S}_{\text{outer}}$). These world tubes $\mathcal{H}_1$, $\mathcal{H}_2$, and $\mathcal{H}_{\text{outer}}$ are the dynamical apparent horizons. One may ask whether additional strictly stable MOTSs may exist if we do not restrict ourselves to only axisymmetric surfaces. Fortunately, this has been ruled out by Theorem 8.1 in Ref. [18]. This unambiguous natural choice of physically relevant horizons provides an additional numerical indication that dynamical apparent horizons are well-behaved objects suitable to describe the highly dynamical and nonperturbative regime during such a merger.

That said, the apparent horizons cannot forever remain aloof from the common herd. $\mathcal{S}_{\text{outer}}$ appears out of a bifurcation with the unstable $\mathcal{S}_{\text{inner}}$ while $\mathcal{S}_2$ and (likely) $\mathcal{S}_1$ are ultimately annihilated in mergers with other unstable MOTSs. The additional MOTTs then significantly increase our understanding of the interior structure forming shortly after the common apparent horizon appears. This structure shares certain features with previous speculations that the merger might, in fact, be described by a single smooth MOTT weaving back and forth in time [14,20–22]. What we find is significantly more complicated: we find *multiple* MOTTs weaving in time, but they do not connect to form a single smooth world tube. Since we lose the MOTSs only for (well understood) numerical reasons, it seems plausible that they continue to weave back and forth, possibly forming more and more self-intersections. We also find that all world tubes seem to be connected.[8] However, since no MOTS crosses a puncture, some connections are not smooth and instead happen via the observed mechanism where two MOTSs touch and their union coincides with a third MOTS having a cusp. This third MOTS subsequently develops a new self-intersection.

Together, these observations motivate the following suggestion. If one assumes that (i) MOTSs cannot cross punctures, (ii) MOTSs appear and disappear only as pairs, (iii) all MOTTs connect in some form[9], and (iv) the individual apparent horizons vanish at some point during

[8]The likely annihilation of $\mathcal{S}_1$ with $\mathcal{S}_1^*$ is discussed in Sec. IV B 3. Similarly, based on our results we expect coincidences of $\mathcal{S}_2^{**}$ with $\mathcal{S}_2 \cup \mathcal{S}_{1a}$ and $\mathcal{S}_0^{**}$ with $\mathcal{S}_{1a} \cup \mathcal{S}_{2a}$ to happen via cusp-formation.

[9]The connection can either be a bifurcation/annihilation or a coincidence of two MOTSs and a MOTS with a cusp.

a merger, then many of the observed behaviors seem to be inevitable. It seems conceivable that (i) holds and the results of Andersson *et al.* [32] point toward (ii). While our results certainly do not *imply* (iii) and (iv), they might still provide an incentive for further investigation in this direction.

The present results for the axisymmetric head-on collision of two black holes also have implications for the generic case where inspiraling black holes coalesce without any symmetry. We now know which kinds of surfaces a generalized MOTS finder must be able to resolve and which surfaces to look for. One might explore whether a generalization of the shooting method could be used to approximate near-axisymmetric MOTSs to be used as initial guesses for such a finder. An important question will be whether it is still only three MOTTs which are stable and hence dynamical apparent horizons.

ACKNOWLEDGMENTS

We would like to express our gratitude to Graham Cox, Jose Luis Jaramillo, Badri Krishnan, Hari Kunduri and the members of the Memorial University Gravity Journal Club for valuable discussions and suggestions. I. B. was supported by the Natural Science and Engineering Research Council of Canada Discovery Grant No. 2018-0473. The work of R. A. H. was supported by the Natural Science and Engineering Research Council of Canada through the Banting Postdoctoral Fellowship program and also by Asian Office of Aerospace Research & Development Grant No. FA2386-19-1-4077.

APPENDIX A: FAMILIES OF SURFACES OF CONSTANT EXPANSION

A MOTS $\mathcal{S}$ is defined as a closed surface with zero outward expansion, $\Theta_+ = 0$. However, one may also try to look for surfaces $\mathcal{S}_c$ with $\Theta_+ = c$, where $c = \text{const}$, in a neighborhood of any given MOTS. These surfaces can be used to help locating common MOTSs as early as possible during the simulation by tracking common surfaces $\mathcal{S}_{c>0}$, which are seen to exist prior to the formation of a common MOTS $\mathcal{S} = \mathcal{S}_{c=0}$ [64,65]. We will show here another application of such surfaces, which turned out to be helpful in resolving the various bifurcations and annihilations. This is related to and motivated by the observation made in [23] that a family of such surfaces may connect one MOTS with another. See Fig. 13 in [23] and its discussion for details.

We start with a MOTS $\mathcal{S}$ found in some particular Cauchy slice Σ_t at simulation time $t = t_1$. This surface is then tracked through the simulation forwards and backwards in time. If in either direction, the MOTS is lost and cannot be located anymore, say at $t_2 > t_1$, then we choose a time $t \lesssim t_2$ and construct a family of surfaces $\mathcal{S}_c$ starting with $\mathcal{S}_0 = \mathcal{S}$. Note that just as there may be multiple MOTSs $\mathcal{S}_0$ in any given Cauchy slice, the surfaces $\mathcal{S}_c$ for $c \neq 0$ will also not be unique in general. However, when varying c in small steps $c \to c' = c + \varepsilon$, one can look for $\mathcal{S}_{c'}$ in the vicinity of $\mathcal{S}_c$ by taking $\mathcal{S}_c$ as initial guess. As an example, Fig. 21 shows such a family in terms of the expansion and area of the $\mathcal{S}_c$. In this case, we start from $\mathcal{S}_2$ at a time $t = 2.5M$ and we are able to reliably locate $\mathcal{S}_2^*$ and $\mathcal{S}_2^{**}$. Figure 22 shows the shapes of these surfaces of constant expansion and how they connect $\mathcal{S}_2$ with $\mathcal{S}_2^*$ (left panel) and $\mathcal{S}_2^*$ with $\mathcal{S}_2^{**}$ (right panel).

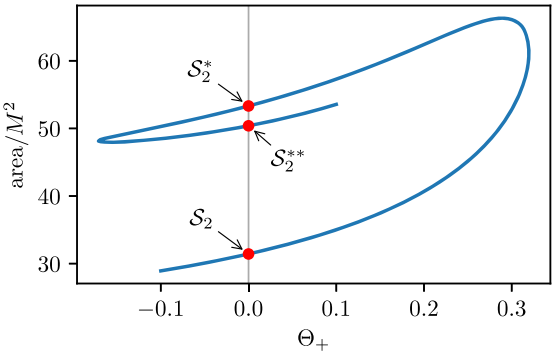

FIG. 21. A family of surfaces of constant expansion shown in the plane of area and expansion. Each point on the solid line corresponds to one surface of this family. Whenever the curve crosses $\Theta_+ = 0$, the surface is a MOTS. This plot shows a family constructed from $\mathcal{S}_2$ at simulation time $t = 2.5M$, which connects $\mathcal{S}_2$ with $\mathcal{S}_2^*$ and $\mathcal{S}_2^{**}$.

A slight complication is encountered whenever $\Theta_+ = c$ has a local extremum. This happens twice in Fig. 21. In these cases we cannot vary c but instead we can take a small step in area by prescribing the area instead of the expansion for this step (see, e.g., [64]). Alternatively, one can *anticipate* the shape change by extrapolating from the previous steps to construct an initial guess surface which overcomes the extremum of c.

Once another MOTS is found this way, it can itself be tracked forwards and backwards in time to resolve the possible annihilation or bifurcation.

APPENDIX B: ANNIHILATION OF $\mathcal{S}_1$ WITH $\mathcal{S}_1^*$

The annihilation of the larger individual MOTS $\mathcal{S}_2$ with $\mathcal{S}_2^*$ was found with high accuracy and is discussed in the main text. Here, the goal is to show that it is plausible that the smaller individual MOTS $\mathcal{S}_1$ also annihilates, in this case with $\mathcal{S}_1^*$, and that it does not have a qualitatively different behavior than $\mathcal{S}_2$ in this regard. To this end, we perform a simulation with different initial conditions than those in the main text and show that both individual horizons annihilate. We take this as suggesting that the lack of annihilation in the main configuration is purely due to the numerical setup and caused by the MOTS moving

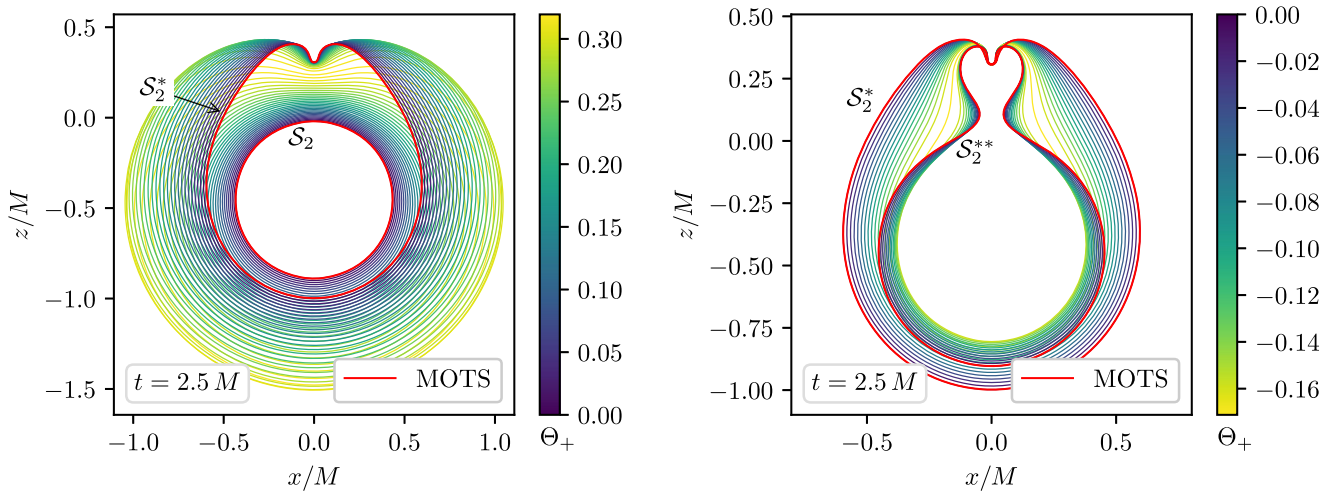

FIG. 22. Shapes of the family of constant expansion surfaces of Fig. 21. Shown is the subset of surfaces connecting $\mathcal{S}_2$ with $\mathcal{S}_2^*$ (left panel) and the subset connecting $\mathcal{S}_2^*$ with $\mathcal{S}_2^{**}$ (right panel). The color indicates the value of $\Theta_+ = c$ while the MOTSs are shown as solid red lines.

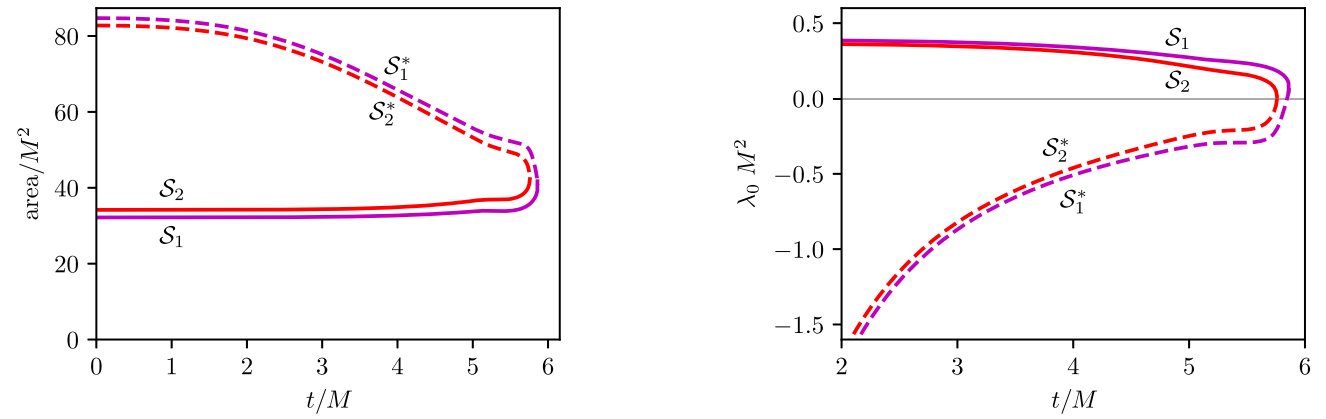

FIG. 23. Evolution of the area (left panel) and principal stability eigenvalue (right panel) for a simulation with initial conditions $q = m_2/m_1 = 1.05$ and $d = 0.4$. We focus here on the individual apparent horizons of $\mathcal{S}_{1,2}$ and the MOTSs with which they annihilate, $\mathcal{S}_1^*$ and $\mathcal{S}_2^*$, respectively. These plots show a simulation with resolution $1/\Delta x = 960$. Note that the final part for $t \gtrsim 5M$ still suffers from the MOTSs being too close to the numerically underresolved puncture regions.

too close to the puncture (in the numerical coordinates) as also analyzed in [59].

By using more equal masses, the shape of the smaller apparent horizon remains larger in coordinates for a longer time, and a smaller initial distance parameter reduces the simulation time when the annihilation takes place. Figure 23 shows the area and principal stability eigenvalue for a simulation with a mass ratio of $q = 1.05$ and distance parameter $d = 0.4$. We see that both individual apparent horizons seem to annihilate, first the larger one $\mathcal{S}_2$ with $\mathcal{S}_2^*$ and shortly after the smaller one $\mathcal{S}_1$ with $\mathcal{S}_1^*$. Despite the above choice of parameters for this simulation, the MOTSs still approach the punctures (in coordinates) before they vanish. We found the annihilations of both apparent horizons in simulations with spatial resolutions of $1/\Delta x = 480$, 720, and 960. However, the precise behavior of these curves in the final time span after $t \sim 5M$ varies between the resolutions. While not as convincing as the remaining results we present, a merger of $\mathcal{S}_1$ and $\mathcal{S}_1^*$ seems at least plausible.

[1] B. P. Abbott *et al.* (LIGO Scientific, Virgo Collaborations), GWTC-1: A Gravitational-Wave Transient Catalog of Compact Binary Mergers Observed by LIGO and Virgo during the First and Second Observing Runs, Phys. Rev. X **9**, 031040 (2019).

[2] B. P. Abbott *et al.* (LIGO Scientific, Virgo Collaborations), Binary Black Hole Mergers in the First Advanced LIGO Observing Run, Phys. Rev. X **6**, 041015 (2016); **8**, 039903(E) (2018).

[3] Alexander H. Nitz, Collin Capano, Alex B. Nielsen, Steven Reyes, Rebecca White, Duncan A. Brown, and Badri Krishnan, 1-OGC: The first open gravitational-wave catalog of binary mergers from analysis of public Advanced LIGO data, Astrophys. J. **872**, 195 (2019).

[4] Alexander H. Nitz, Thomas Dent, Gareth S. Davies, Sumit Kumar, Collin D. Capano, Ian Harry, Simone Mozzon, Laura Nuttall, Andrew Lundgren, and Márton Tápai, 2-OGC: Open gravitational-wave catalog of binary mergers from analysis of public Advanced LIGO and Virgo data, Astrophys. J. **891**, 123 (2019).

[5] Alexander H. Nitz, Thomas Dent, Gareth S. Davies, and Ian Harry, A search for gravitational waves from binary mergers with a single observatory, Astrophys. J. **897**, 169 (2020).

[6] Tejaswi Venumadhav, Barak Zackay, Javier Roulet, Liang Dai, and Matias Zaldarriaga, New binary black hole mergers in the second observing run of Advanced LIGO and Advanced Virgo, Phys. Rev. D **101**, 083030 (2020).

[7] Barak Zackay, Tejaswi Venumadhav, Liang Dai, Javier Roulet, and Matias Zaldarriaga, Highly spinning and aligned binary black hole merger in the Advanced LIGO first observing run, Phys. Rev. D **100**, 023007 (2019).

[8] Geraint Pratten *et al.*, Let's twist again: Computationally efficient models for the dominant and sub-dominant harmonic modes of precessing binary black holes, Phys. Rev. D **103**, 104056 (2021).

[9] Vijay Varma, Scott E. Field, Mark A. Scheel, Jonathan Blackman, Davide Gerosa, Leo C. Stein, Lawrence E. Kidder, and Harald P. Pfeiffer, Surrogate models for precessing binary black hole simulations with unequal masses, Phys. Rev. Research **1**, 033015 (2019).

[10] S. W. Hawking and J. B. Hartle, Energy and angular momentum flow into a black hole, Commun. Math. Phys. **27**, 283 (1972).

[11] Abhay Ashtekar and Badri Krishnan, Isolated and dynamical horizons and their applications, Living Rev. Relativity **7**, 10 (2004).

[12] Valerio Faraoni and Angus Prain, Understanding dynamical black hole apparent horizons, Lect. Notes Phys. **907**, 1 (2015).

[13] Ivan Booth, Black hole boundaries, Can. J. Phys. **83**, 1073 (2005).

[14] Sean A. Hayward, Black holes: New horizons, in *Recent Developments in Theoretical and Experimental General Relativity, Gravitation and Relativistic Field Theories, Proceedings of the 9th Marcel Grossmann Meeting, MG'9, Rome, Italy, 2000, Pts. A-C* (World Scientific, Singapore, 2000), pp. 568–580.

[15] Badri Krishnan, Fundamental properties and applications of quasi-local black hole horizons, Classical Quantum Gravity **25**, 114005 (2008).

[16] Abhay Ashtekar and Badri Krishnan, Dynamical horizons and their properties, Phys. Rev. D **68**, 104030 (2003).

[17] Lars Andersson, Marc Mars, and Walter Simon, Local Existence of Dynamical and Trapping Horizons, Phys. Rev. Lett. **95**, 111102 (2005).

[18] Lars Andersson, Marc Mars, and Walter Simon, Stability of marginally outer trapped surfaces and existence of marginally outer trapped tubes, Adv. Theor. Math. Phys. **12**, 853 (2008).

[19] Ishai Ben-Dov, Penrose inequality and apparent horizons, Phys. Rev. D **70**, 124031 (2004).

[20] Ivan Booth, Lionel Brits, Jose A. Gonzalez, and Chris Van Den Broeck, Marginally trapped tubes and dynamical horizons, Classical Quantum Gravity **23**, 413 (2006).

[21] P. Mösta, L. Andersson, J. Metzger, B. Szilágyi, and J. Winicour, The merger of small and large black holes, Classical Quantum Gravity **32**, 235003 (2015).

[22] Anshu Gupta, Badri Krishnan, Alex Nielsen, and Erik Schnetter, Dynamics of marginally trapped surfaces in a binary black hole merger: Growth and approach to equilibrium, Phys. Rev. D **97**, 084028 (2018).

[23] Daniel Pook-Kolb, Ofek Birnholtz, Badri Krishnan, and Erik Schnetter, Existence and stability of marginally trapped surfaces in black-hole spacetimes, Phys. Rev. D **99**, 064005 (2019).

[24] Jonathan Thornburg, Event and apparent horizon finders for $3+1$ numerical relativity, Living Rev. Relativity **10**, 3 (2007).

[25] Daniel Pook-Kolb, Ofek Birnholtz, Badri Krishnan, and Erik Schnetter, Interior of a Binary Black Hole Merger, Phys. Rev. Lett. **123**, 171102 (2019).

[26] Daniel Pook-Kolb, Ofek Birnholtz, Badri Krishnan, and Erik Schnetter, Self-intersecting marginally outer trapped surfaces, Phys. Rev. D **100**, 084044 (2019).

[27] Daniel Pook-Kolb, Ofek Birnholtz, José Luis Jaramillo, Badri Krishnan, and Erik Schnetter, Horizons in a binary black hole merger I: Geometry and area increase, arXiv:2006.03939.

[28] Daniel Pook-Kolb, Ofek Birnholtz, José Luis Jaramillo, Badri Krishnan, and Erik Schnetter, Horizons in a binary black hole merger II: Fluxes, multipole moments and stability, arXiv:2006.03940.

[29] Ivan Booth, Robie A. Hennigar, and Daniel Pook-Kolb, preceding paper, Ultimate fate of apparent horizons during a binary black hole merger I: Locating and understanding axisymmetric marginally outer trapped surfaces, Phys. Rev. D 084083 (2021).

[30] D. Pook-Kolb, R. A. Hennigar, and I. Booth, companion Letter, What Happens to Apparent Horizons in a Binary Black Hole Merger?, Phys. Rev. Lett. **127**, 181101 (2021).

[31] Roger Penrose, Gravitational Collapse and Space-time Singularities, Phys. Rev. Lett. **14**, 57 (1965).

[32] Lars Andersson, Marc Mars, Jan Metzger, and Walter Simon, The time evolution of marginally trapped surfaces, Classical Quantum Gravity **26**, 085018 (2009).

[33] Abhay Ashtekar and Gregory J. Galloway, Some uniqueness results for dynamical horizons, Adv. Theor. Math. Phys. **9**, 1 (2005).

[34] Abhay Ashtekar and Badri Krishnan, Dynamical Horizons: Energy, Angular Momentum, Fluxes and Balance Laws, Phys. Rev. Lett. **89**, 261101 (2002).

[35] Ivan Booth, Robie A. Hennigar, and Saikat Mondal, Marginally outer trapped surfaces in the Schwarzschild spacetime: Multiple self-intersections and extreme mass ratio mergers, Phys. Rev. D **102**, 044031 (2020).
[36] José Luis Jaramillo, Black hole horizons and quantum charged particles, Classical Quantum Gravity **32**, 132001 (2015).
[37] R. P. A. C. Newman, Topology and stability of marginal 2-surfaces, Classical Quantum Gravity **4**, 277 (1987).
[38] S. A. Hayward, General laws of black hole dynamics, Phys. Rev. D **49**, 6467 (1994).
[39] Raphael Bousso and Netta Engelhardt, New Area Law in General Relativity, Phys. Rev. Lett. **115**, 081301 (2015).
[40] Abhay Ashtekar, Jonathan Engle, Tomasz Pawłowski, and Chris Van Den Broeck, Multipole moments of isolated horizons, Classical Quantum Gravity **21**, 2549 (2004).
[41] Dieter R. Brill and Richard W. Lindquist, Interaction energy in geometrostatics, Phys. Rev. **131**, 471 (1963).
[42] Daniel Pook-Kolb, Ofek Birnholtz, Ivan Booth, Robie A. Hennigar, José Luis Jaramillo, Badri Krishnan, Erik Schnetter, and Victor Zhang, MOTS Finder version 1.5 (Zenodo, 2021), https://doi.org/10.5281/zenodo.4687700.
[43] Erik Schnetter and Jonah Miller, eschnett/SimulationIO: New release to trigger Zenodo (Zenodo, 2019), https://doi.org/10.5281/zenodo.3258858.
[44] Mike Boyle, Spinsfast: Fast and exact spin-s spherical-harmonic transforms (Zenodo, 2018), https://doi.org/10.5281/zenodo.1221354.
[45] Pauli Virtanen *et al.*, (SciPy 1.0 Contributors), SciPy 1.0: Fundamental algorithms for scientific computing in Python, Nat. Methods **17**, 261 (2020).
[46] S. van der Walt, S. C. Colbert, and G. Varoquaux, The NumPy array: A structure for efficient numerical computation, Comput. Sci. Eng. **13**, 22 (2011).
[47] Fredrik Johansson *et al.*, mpmath: A Python library for arbitrary-precision floating-point arithmetic (version 1.1.0) (2018), http://mpmath.org/.
[48] Aaron Meurer, Christopher P. Smith, Mateusz Paprocki, Ondřej Čertík, Sergey B. Kirpichev, Matthew Rocklin, AMiT Kumar, Sergiu Ivanov, Jason K. Moore, Sartaj Singh *et al.*, SymPy: Symbolic computing in Python, PeerJ Comput. Sci. **3**, e103 (2017).
[49] J. D. Hunter, Matplotlib: A 2d graphics environment, Comput. Sci. Eng. **9**, 90 (2007).
[50] Michael Droettboom *et al.*, matplotlib/matplotlib v2.2.2 (Zenodo, 2018), https://doi.org/10.5281/zenodo.1202077.
[51] Frank Löffler, Joshua Faber, Eloisa Bentivegna, Tanja Bode, Peter Diener, Roland Haas, Ian Hinder, Bruno C. Mundim, Christian D. Ott, Erik Schnetter, Gabrielle Allen, Manuela Campanelli, and Pablo Laguna, The Einstein toolkit: A community computational infrastructure for relativistic astrophysics, Classical Quantum Gravity **29**, 115001 (2012).
[52] EinsteinToolkit, Einstein Toolkit: Open software for relativistic astrophysics, http://einsteintoolkit.org/.
[53] Marcus Ansorg, Bernd Brügmann, and Wolfgang Tichy, A single-domain spectral method for black hole puncture data, Phys. Rev. D **70**, 064011 (2004).
[54] J. David Brown, Peter Diener, Olivier Sarbach, Erik Schnetter, and Manuel Tiglio, Turduckening black holes: An analytical and computational study, Phys. Rev. D **79**, 044023 (2009).
[55] Sascha Husa, Ian Hinder, and Christiane Lechner, Kranc: A Mathematica application to generate numerical codes for tensorial evolution equations, Comput. Phys. Commun. **174**, 983 (2006).
[56] Kranc, Kranc: Kranc assembles numerical code, http://kranccode.org/.
[57] Miguel Alcubierre, Gabrielle Allen, Bernd Brügmann, Thomas Dramlitsch, Jose A. Font, Philippos Papadopoulos, Edward Seidel, Nikolaos Stergioulas, Wai-Mo Suen, and Ryoji Takahashi, Towards a stable numerical evolution of strongly gravitating systems in general relativity: The conformal treatments, Phys. Rev. D **62**, 044034 (2000).
[58] Miguel Alcubierre, Bernd Brügmann, Peter Diener, Michael Koppitz, Denis Pollney, Edward Seidel, and Ryoji Takahashi, Gauge conditions for long term numerical black hole evolutions without excision, Phys. Rev. D **67**, 084023 (2003).
[59] Christopher Evans, Deborah Ferguson, Bhavesh Khamesra, Pablo Laguna, and Deirdre Shoemaker, Inside the final black hole: Puncture and trapped surface dynamics, Classical Quantum Gravity **37**, 15LT02 (2020).
[60] Gregory B. Cook and Andrew M. Abrahams, Horizon structure of initial-data sets for axisymmetric two-black-hole collisions, Phys. Rev. D **46**, 702 (1992).
[61] Erik Schnetter, Badri Krishnan, and Florian Beyer, Introduction to dynamical horizons in numerical relativity, Phys. Rev. D **74**, 024028 (2006).
[62] Pierre Mourier, Xisco Jimenez-Forteza, Daniel Pook-Kolb, Badri Krishnan, and Erik Schnetter, Quasinormal modes and their overtones at the common horizon in a binary black hole merger, Phys. Rev. D **103**, 044054 (2021).
[63] Raphael Bousso and Netta Engelhardt, Proof of a new area law in general relativity, Phys. Rev. D **92**, 044031 (2015).
[64] Erik Schnetter, Finding apparent horizons and other two surfaces of constant expansion, Classical Quantum Gravity **20**, 4719 (2003).
[65] Erik Schnetter, Frank Herrmann, and Denis Pollney, Horizon pretracking, Phys. Rev. D **71**, 044033 (2005).